Chem

Article

Electrochemical ^{6}Li isotope enrichment based on selective insertion in 1D tunnel-structured V_2O_5

Graphical abstract

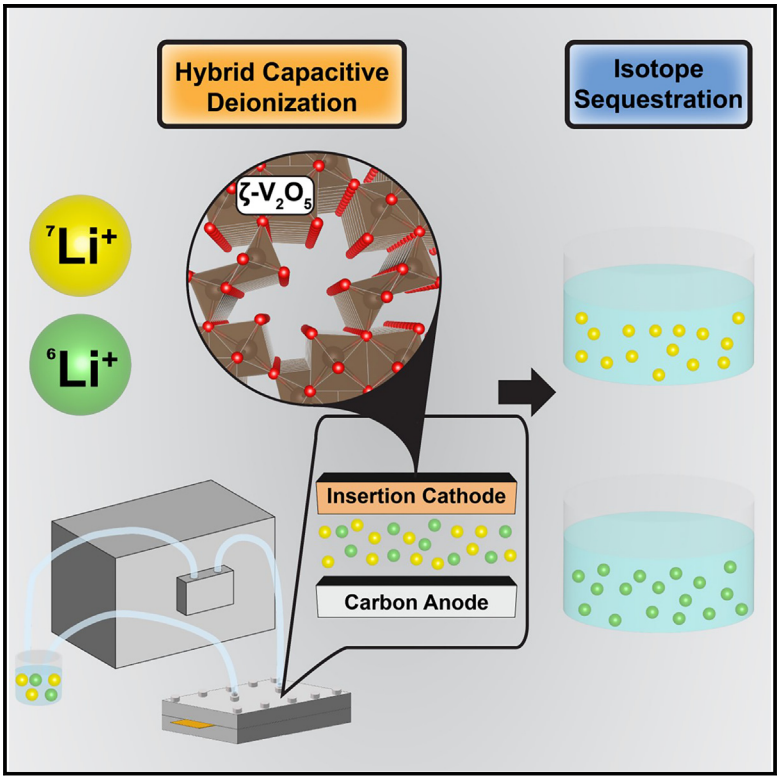

Highlights

- Li ions inserted within 1D tunnels of ζ-V_2O_5
- Electrochemical ^{6}Li enrichment comparable to mercury amalgam process
- *In situ* X-ray microscopy showing reversible Li-ion insertion
- Selective isotope sequestration traceable to specific Li coordination environments

Authors

J. Luis Carrillo, Andrew A. Ezazi, Saul Perez-Beltran, ..., Lucia Zuin, Jian Wang, Sarbajit Banerjee

Correspondence

sbanerje@ethz.ch

In brief

The renaissance of nuclear energy is predicated on the availability of ^{6}Li for nuclear bombardment reactions to produce tritium fuel in breeder reactors. However, the low natural abundance of ^{6}Li represents a substantial challenge. In this article, Carrillo et al. demonstrate an electrochemical approach to enrich ^{6}Li from aqueous flow streams based on insertion of Li ions in a metastable polymorph of V_2O_5 characterized by a 1D tunnel. The process overcomes the performance, toxicity, and sustainability concerns of conventional mercury-amalgam-based separation methods.

Carrillo et al., 2025, Chem *11*, 102486
August 14, 2025
https://doi.org/10.1016/j.chempr.2025.102486

CellPress

Please cite this article in press as: Carrillo et al., Electrochemical ^{6}Li isotope enrichment based on selective insertion in 1D tunnel-structured V_2O_5, Chem (2025), https://doi.org/10.1016/j.chempr.2025.102486

Chem

CellPress

Article

Electrochemical ^{6}Li isotope enrichment based on selective insertion in 1D tunnel-structured V_2O_5

J. Luis Carrillo,[1,2,8] Andrew A. Ezazi,[1,2,8] Saul Perez-Beltran,[1,2,8] Carlos A. Larriuz,[1,2] Harris Kohl,[1,2] Jaime A. Ayala,[1,2] Arnab Maji,[1,2] Stanislav Verkhoturov,[1] Mohammed Al-Hashimi,[3] Hassan Bazzi,[3] Conan Weiland,[4] Cherno Jaye,[4] Daniel A. Fischer,[4] Lucia Zuin,[5] Jian Wang,[5] and Sarbajit Banerjee[1,2,6,7,9,*]

[1]Department of Chemistry, Texas A&M University, College Station, TX 77842-3012, USA
[2]Department of Materials Science and Engineering, Texas A&M University, College Station, TX 77843-3003, USA
[3]College of Science and Engineering, Hamad Bin Khalifa University, P.O. Box 34110, Doha, Qatar
[4]Material Measurement Laboratory, National Institute of Standards and Technology, Gaithersburg, MD 20899, USA
[5]Canadian Light Source Inc., 44 Innovation Boulevard, Saskatoon, SK S7N 2V3, Canada
[6]Laboratory for Inorganic Chemistry, Department of Chemistry and Applied Biosciences, ETH Zurich, Vladimir-Prelog-Weg 2, 8093 Zürich, Switzerland
[7]Laboratory for Battery Science, PSI Center for Energy and Environmental Sciences, Paul Scherrer Institute, Forschungsstrasse 111, 5232 Villigen, Switzerland
[8]These authors contributed equally
[9]Lead contact
*Correspondence: sbanerje@ethz.ch
https://doi.org/10.1016/j.chempr.2025.102486

THE BIGGER PICTURE Nascent efforts to develop fusion energy at scale require the scalable production of isotopically pure ^{6}Li as a target for nuclear bombardment reactions to produce tritium fuel. Conventional approaches to extract low-abundance ^{6}Li from natural abundance sources rely on mercury amalgams and are constrained by concerns related to toxicity, sustainability, and performance. In this article, Carrillo et al. report selective electrochemical ^{6}Li isotope separation from aqueous flow streams using ζ-V_2O_5, a metastable polymorph of V_2O_5. Synchrotron-based *in situ* X-ray microscopy and hard X-ray photoemission spectroscopy corroborate Li-ion insertion within the 1D tunnels of ζ-V_2O_5. Single-cycle enrichment values are comparable with state-of-the-art methods. By coupling with inexpensive renewable energy, the rapid production at scale of isotopically enriched lithium from natural abundance feedstocks will enable significant expansion of nuclear fusion.

SUMMARY

The renaissance of nuclear energy has generated substantial demand for ^{6}Li as a target for nuclear bombardment reactions to produce tritium fuel in breeder reactors. Conventional isotope separation methods utilize differential solubility in mercury amalgams, which pose performance, toxicity, and sustainability concerns. Here, we show that hybrid capacitive deionization wherein Li ions are inserted from aqueous media within the 1D tunnels of a metastable polymorph, ζ-V_2O_5, can be used to selectively sequester ^{6}Li ions. An enrichment factor of ca. 57‰ is achieved. X-ray scattering, spectroscopy, and operando spectromicroscopy studies indicate that Li ions are sequestered within 1D tunnels of ζ-V_2O_5 through faradaic processes. ^{6}Li and ^{7}Li ions are found to migrate at different rates because of subtly different coordination environments. The results illustrate that ζ-V_2O_5 can be utilized as a discriminating host to selectively sequester and enrich ^{6}Li from natural abundance precursor flow streams and suggest a distinctive mode of achieving viable isotope separation.

INTRODUCTION

Promising advancements in nuclear fusion have sparked renewed interest in ^{6}Li production for tritium breeding.[1–3] Modern fusion reactors are designed to utilize deuterium—tritium fuel mixtures, where tritium is generated within "breeding blankets" through nuclear bombardment of precursors such as ^{6}Li.[1] Tritium production from ^{6}Li is preferred since it only requires a singular neutron collision event. However, separation and enrichment of the lighter lithium (Li) isotope poses significant

Please cite this article in press as: Carrillo et al., Electrochemical ^{6}Li isotope enrichment based on selective insertion in 1D tunnel-structured V_2O_5, Chem (2025), https://doi.org/10.1016/j.chempr.2025.102486

challenges. The conventional Li isotope separation method, the COLEX process, involves counter-flowing liquid mercury against an aqueous LiOH solution[4] to yield a ^{6}Li-enriched mercury amalgam and a residual ^{7}Li-enriched LiOH aqueous flow stream. The COLEX process, however, is hampered by its complexity, environmental impact, and low efficiency, which presents a substantial bottleneck to the advancement of nuclear fusion. Since domestic production of ^{6}Li ceased in 1963 as a result of mercury pollution concerns, the United States has relied almost exclusively on a stockpile maintained at Oak Ridge National Laboratory.[5] As such, developing alternative approaches to ^{6}Li enrichment represents an urgent imperative to alleviate materials criticality concerns and to address a critical roadblock to nuclear energy.

Modern Li isotope enrichment processes rely on subtle differences in Li binding affinities.[6–8] Most available processes yield low enrichment coefficients and require prohibitive amounts of solvent or expensive reagents such as crown ethers.[9,10] Alternatively, electrochemical separation methods, which rely on overpotential differentials, are hindered by slow reaction kinetics.[11] For instance, while electrodeposition of Li metal shows promising enrichment factors, its practical application is limited by the large voltages needed to drive the reduction to Li metal as well as the need for Li metal electrocrystallization, which is plagued by substantial safety concerns. Thus, the design of alternative separation methods has emerged as a pressing need. Here, we present a novel approach to ^{6}Li enrichment using hybrid capacitive deionization (HCDI), which is based on the selective isotope insertion and binding of ^{6}Li within the 1D tunnels of a metastable V_2O_5 polymorph, ζ-V_2O_5.

In comparison to CDI, where electrochemical ion separation is achieved through the electroabsorbtion of ions from flow streams onto high-surface-area (typically) carbon electrodes,[12–16] HCDI involves ion storage within a redox-active insertion host based on faradaic reactions. While HCDI leverages a similar configuration to traditional CDI, the high-surface-area-activated carbon at the positive electrode is replaced by an insertion host.[17,18] This setup enables utilization of the entire volume of the material through activation of capacitative, pseudocapacitative, and faradaic processes, thereby enabling ion storage beyond just particle surfaces.[19,20] Additionally, ion selectivity is significantly enhanced as a result of the insertion preferences of ions in specific interstitial sites of host materials.[21] We have previously reported that ζ-V_2O_5, a metastable polymorph of V_2O_5, acts as an insertion host capable of extracting Li from aqueous flow streams.[22] With ζ-V_2O_5, we have demonstrated electrochemical sequestration of ions from challenging sources such as oilfield-produced water from the Permian Basin. Notably, ζ-V_2O_5 exhibits a significant preference for Li over other dissolved alkali- and alkaline-earth cations.[23] In this work, we demonstrate the remarkable isotopic enrichment of ^{6}Li from an unenriched feed stream. We characterize HCDI-lithiated ζ-V_2O_5 using powder X-ray diffraction (XRD), hard X-ray photoemission spectroscopy (HAXPES), X-ray absorption near-edge structure (XANES) spectroscopy, Raman spectroscopy, and *in situ* scanning transmission X-ray microscopy (STXM) to confirm the insertion of Li ions within the 1D tunnels of ζ-V_2O_5. We further investigate ^{6}Li enrichment using secondary ion mass spectrometry (SIMS) and *ab initio* molecular dynamics (AIMD) simulations.

RESULTS AND DISCUSSION

Li sequestration within 1D tunnels of ζ-V_2O_5

In contrast to the single-layered thermodynamic orthorhombic α-V_2O_5 polymorph, where Li-ion insertion brings about a series of distortive structural transformations as exemplified in Figure S1, increased concentrations of Li ions are accommodated in the 1D tunnels of ζ-V_2O_5 through cation reordering.[22] High-resolution structure solutions from single-crystal XRD have identified four distinct interstitial sites that can accommodate Li ions, which are labeled in Figure 1A as β, β', C, and I sites.[21] ζ-V_2O_5 porous electrodes are assembled within an HCDI cell (Figure 1D) and chronoamperometry is performed while flowing an aqueous solution of lithium chloride (LiCl); measurements of solution conductivity are performed in parallel and translated to Li concentrations based on calibration curves. Electrode samples are recovered at different points as indicated in Figure 1D, and they are analyzed using a suite of X-ray scattering, spectroscopy, and spectromicroscopy tools to evidence that Li ions are sequestered within the 1D tunnels of ζ-V_2O_5 (and not just adsorbed onto particle surfaces), demonstrating the key role of faradaic processes in underpinning ion storage, and to quantify the concentration of ions sequestered in the electrodes.

HCDI-recovered samples are benchmarked to ζ-V_2O_5 samples that have been topochemically lithiated as per Equation 9 to assess the extent and mode of lithiation. Figure 1B shows color changes of ζ-V_2O_5 powders associated with alterations in the oxidation states of the vanadium centers. When the metastable 1D tunnel-structured ζ-V_2O_5 framework is lithiated, faradaic processes result in the reduction of nominally pentavalent vanadium to formally tetravalent vanadium ions, which brings about a color change from bright yellow to dark olive green ascribed to the introduction of midgap defect states.[24] In insulating V_2O_5 polymorphs, reduction of the vanadium centers yields small polarons localized on vanadium sites,[25] as such d-d transitions (intervalence charge transfer bands[26]) and allowed transitions from localized midgap states to the conduction band (formally, metal ligand charge transfer bands) become accessible upon Li-ion insertion and bring about a pronounced change in visible coloration.[27] At high Li-ion concentrations, increasing electronic conductivity imparts a lustrous appearance to individual particles and single crystals.[28] The color change is reversible upon delithiation, which can be done through treating lithiated V_2O_5 powders with $NOBF_4$ or NO_2BF_4 solutions in acetonitrile.[28] This drastic color change has the potential to be used for colorimetric sensing of state of charge of the HCDI active element.[29]

Figures 1C and 1E contrast powder XRD patterns for topochemically lithiated ζ-V_2O_5 and HCDI-recovered positive electrode materials, respectively. Powder XRD patterns for topochemically lithiated ζ-V_2O_5 demonstrate preservation of the 1D ζ-V_2O_5 framework (crystallized in a monoclinic C2/m structure) with increasing lithiation. Rietveld refinements of the diffraction patterns have been used to determine unit cell volumes, which are plotted as a function of Li concentration (determined by

Please cite this article in press as: Carrillo et al., Electrochemical ^{6}Li isotope enrichment based on selective insertion in 1D tunnel-structured V_2O_5, Chem (2025), https://doi.org/10.1016/j.chempr.2025.102486

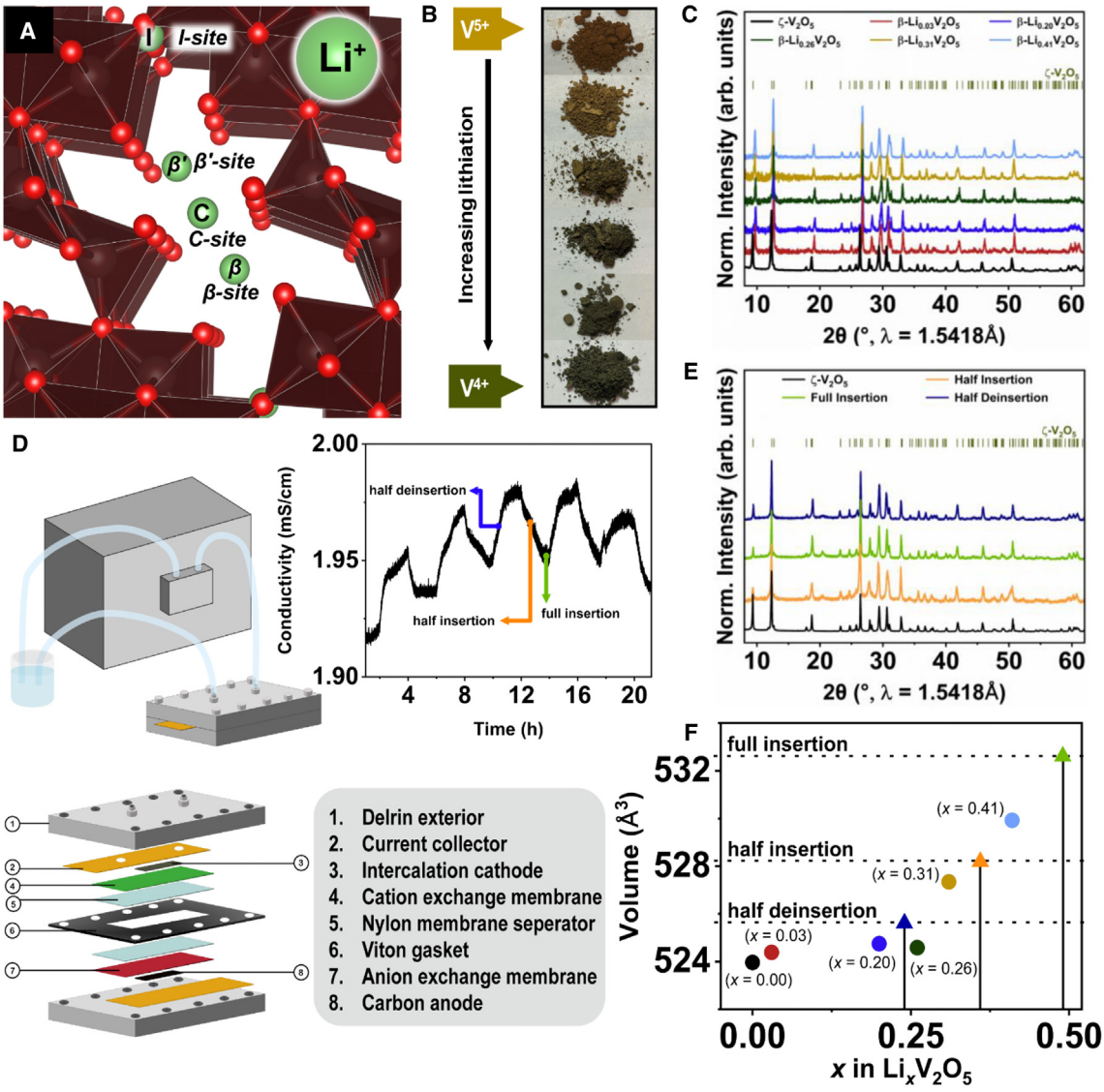

Figure 1. Structural aspects of lithiation-ion sequestration in 1D tunnels of ζ-V_2O_5

(A) Crystal structure of ζ-V_2O_5 illustrating interstitial sites arrayed along a 1D tunnel defined by interconnected [VO_6] octahedra and [VO_5] square pyramids.

(B) Changes in the appearance and coloration of ζ-V_2O_5 powders with increasing topochemical lithiation upon reaction with LiI in acetonitrile.

(C) Powder XRD patterns of topochemically lithiated ζ-V_2O_5 reacted with stoichiometric amounts of LiI; the Li stoichiometries are determined by ICP-MS.

(D) Schematic illustration of HCDI cell and representative conductivity plot denoting points, half insertion, full insertion, and half deinsertion, at which samples are recovered for analysis.

(E) Powder XRD patterns of HCDI-recovered electrodes after Li-ion capture from a 15 mmol/L aqueous solution of LiCl flowed at a rate of 20 mL/min.

(F) Plot of unit cell volume (as determined from Rietveld refinements to powder XRD patterns) versus extent of lithiation determined by ICP-MS. Data points corresponding to ζ-V_2O_5, β-$Li_{0.03}V_2O_5$, β-$Li_{0.20}V_2O_5$, β-$Li_{0.26}V_2O_5$, β-$Li_{0.31}V_2O_5$, β′-$Li_{0.41}V_2O_5$, half insertion, full insertion, and half deinsertion are marked on the plot.

inductively coupled plasma mass spectrometry [ICP-MS]) in Figure 1F. Lattice parameters obtained from the Rietveld refinements are presented in Table S1. A sharp uptick of unit cell volume at a nominal Li concentration of $x \approx 0.33$ in $Li_xV_2O_5$ reflects Li-ion reordering from more capacious seven-coordinated β sites to closely spaced five-coordinated β′ sites arrayed along the 1D tunnel.[21] Markers for volumetric changes derived from Rietveld-refined XRD patterns map the extent of lithiation/deli-thiation in both the topochemically lithiated ζ-V_2O_5, and HCDI-recovered electrode materials are shown in Figure 1F. ICP-MS results for topochemically lithiated and HCDI-recovered samples are provided in Table S2. Powder XRD serves as a reliable probe of the extent of Li ions sequestered within the 1D tunnels for the HCDI-recovered electrode samples since ICP-MS results reflect both inserted and surficial Li. The powder XRD results in Figure 1E thus confirm that Li ions are indeed sequestered

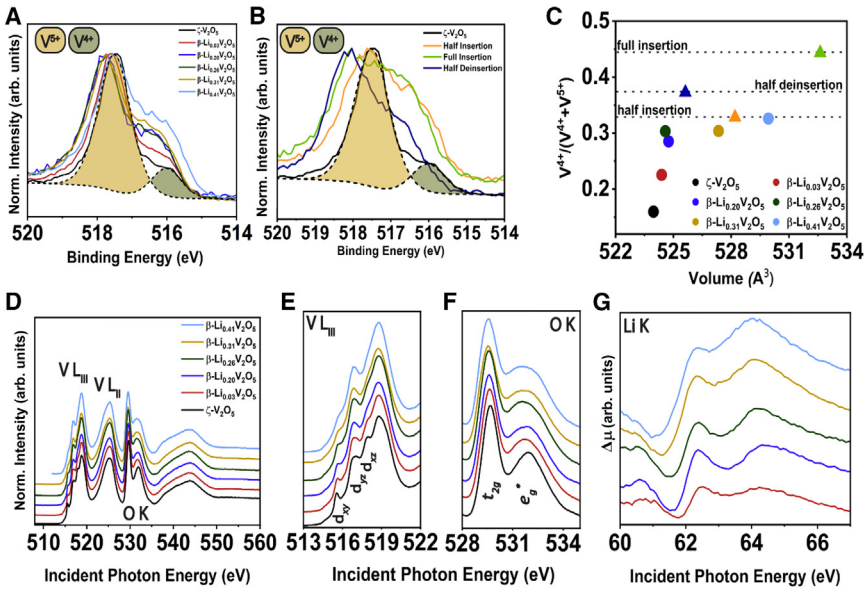

Figure 2. X-ray spectroscopy evaluation of nominal oxidation states of ζ-V_2O_5 and differentiation of capacitative and faradaic processes

(A and B) V $2p_{1/2}$ core-level HAXPES spectra acquired at an incident energy of 2 keV for (A) topochemically lithiated ζ-V_2O_5 prepared by reaction with LiI as per Equation 9 and (B) HCDI-recovered ζ-V_2O_5 upon Li-ion sequestration from a 15 mmol/L aqueous solution of LiCl flowed at a rate of 20 mL/min. The lithium stoichiometries for topochemically lithiated samples have been determined by ICP-MS.

(C) Plot of integrated intensities of $V^{4+}/(V^{4+} + V^{5+})$ core-level HAXPES features denoting operation of faradaic ion storage mechanisms in Li-ion sequestration from aqueous streams by ζ-V_2O_5.

(D–G) (D) V L- and O K-edge XANES spectra acquired for topochemically lithiated ζ-V_2O_5 up to Li stoichiometries of β′-$Li_{0.41}V_2O_5$; (E) magnified view of V L_{III}-edge XANES spectra acquired for topochemically lithiated ζ-V_2O_5 up to Li stoichiometries of β′-$Li_{0.41}V_2O_5$; (F) magnified view of O K-edge XANES spectra acquired for topochemically lithiated ζ-V_2O_5 up to Li stoichiometries of β′-$Li_{0.41}V_2O_5$; (G) difference in Li K-edge XANES spectra acquired for topochemically lithiated ζ-V_2O_5 up to Li stoichiometries of β′-$Li_{0.41}V_2O_5$. For Li K-edge spectra, the spectrum measured for ζ-V_2O_5 has been subtracted to obtain the Δμ XANES spectrum.

from aqueous flow streams within interstitial sites arrayed along 1D tunnels of ζ-V_2O_5. Additional corroboration that HCDI brings about Li-ion insertion within the 1D tunnels of ζ-V_2O_5, as opposed to just at particle surfaces, is derived from Raman spectroscopy measurements. Surface Li-ion absorption is not anticipated to strongly modify the phonon dispersion, whereas Li-ion insertion profoundly alters lattice symmetry.[22,30] Raman spectra for topochemically lithiated ζ-V_2O_5 and HCDI-recovered positive electrode samples are contrasted in Figure S2. Raman assignments are surmised based on comparisons to Raman modes of orthorhombic α-V_2O_5.[28,31] Modes at ca. 140 cm^{-1} correspond to displacements of vanadium-centered polyhedra with respect to each other.[32] Upon increasing Li insertion, the tunnels expand to incorporate Li ions; increasing bond lengths between vanadium centers and extensive disorder as a result of partial Li occupancies in interstitial sites diminish the intensity of this Raman feature. Modes at ca. 290 cm^{-1} correspond to apical V–O bond rocking modes,[31] which are enhanced with increasing lithiation. HCDI-derived positive electrodes recovered at different points show spectral signatures analogous to topochemically lithiated ζ-V_2O_5 (Figure S3B). These results corroborate that ion storage from aqueous flow streams in HCDI is achieved through Li-ion insertion into the 1D tunnels of ζ-V_2O_5.

Operation of faradaic processes

We next analyzed changes in the formal vanadium oxidation state in HCDI-recovered positive electrodes to differentiate capacitative and faradaic processes. In contrast to surface-sensitive XPS, HAXPES measurements performed at an incident photon energy of 2 keV have a penetration depth of (20 to 30 nm), which enables evaluation of not just surface adsorption but also serves as an excellent probe of bulk redox.[32,33] Figures 2A and 2B contrast the evolution of the V $2p_{3/2}$ core-level photoemission spectrum with increasing lithiation for topochemically lithiated and HCDI-recovered ζ-V_2O_5, respectively. Peak fits to pentavalent and tetravalent vanadium, with features centered at 517.5 and 516.6 eV, respectively, are illustrated for ζ-V_2O_5 in each panel. With increasing lithiation, the lower binding energy feature gains spectral weight, denoting a greater extent of vanadium reduction concomitant with Li insertion in ζ-V_2O_5.[23,34] These results provide a clear indication that Li ions are sequestered from aqueous flow streams within the tunnels of the metastable polymorph through the operation of faradaic processes. Figure 2C shows a plot of the $V^{4+}/(V^{4+} + V^{5+})$ integrated intensities with increasing topochemical lithiation; markers for the HCDI-recovered samples corroborate the operation of faradaic processes as the primary mechanism underpinning ion storage. XANES spectroscopy serves as an element-specific probe of partially occupied and unoccupied states and provides insights into nominal oxidation states and electronic structure of V_2O_5 as a function of Li-ion insertion.[35,36] V L- and O K-edge XANES spectra have been acquired for topochemically lithiated ζ-V_2O_5 (Figures 2D and 2F). At the V L_{III}-edge, transitions from V 2*p* core levels to V $3d_{xy}$, $3d_{yz}$, and $3d_{xz}$ hybrid states are observed at 515.5, 517, and 518.1 eV, respectively.[35–39] With increasing lithiation, the V $3d_{xy}$ feature at the conduction band minimum is diminished as a result of Pauli blocking, which reflects the localized reduction of vanadium centers (as also manifested by the pronounced change in color visible in Figure 1B).[37] In turn, O K-edge spectra, which reflect transitions from O 1*s* core levels to O 2*p*–V 3*d* hybrid states, split by crystal field splitting, exhibit distinctive t_{2g} and e_g^* manifolds centered at 529.5 and 532 eV, respectively.[36,39] With increasing lithiation, broadening and renormalization of relative intensities of these features are observed as a result of the lifting of spin degeneracy upon vanadium

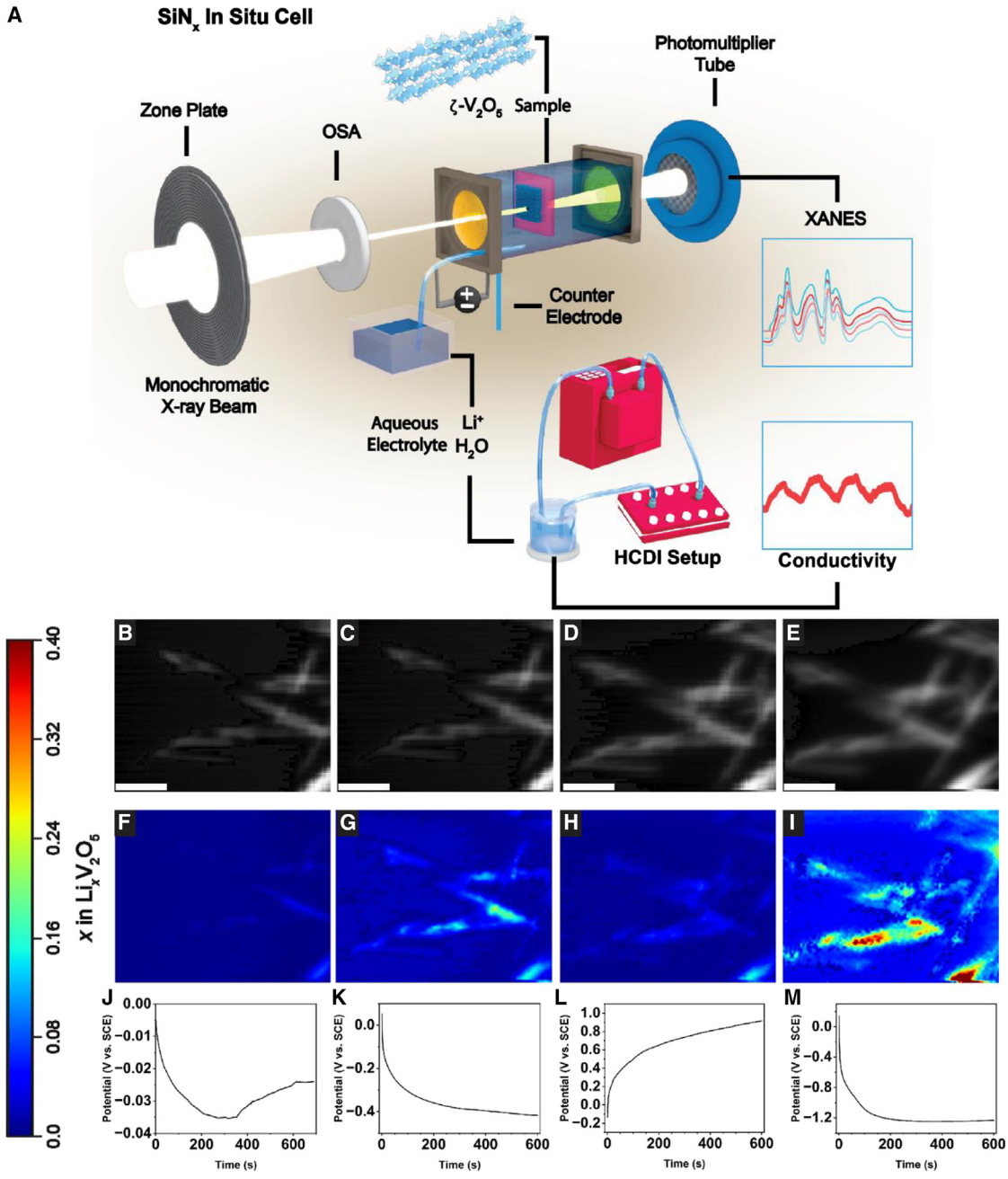

Figure 3. *In situ* imaging of lithium-ion sequestration in individual particles of ζ-V_2O_5

(A) Schematic illustration of experimental setup for *in situ* STXM with ζ-V_2O_5 particles as the working electrode and a flowing aqueous lithium electrolyte emulating the construction of the HCDI cell in Figure 1B.

(B–E) Integrated X-ray optical density maps for unlithiated, cycle 1 reduced (at 1 nA reductive current for 600 s), cycle 1 oxidized (1 nA oxidative current for 600 s), and cycle 2 reduced (2 nA reductive current for 600 s), respectively. All scale bars represent 1 μm.

(F–I) Corresponding composition maps indicating extent of lithiation as per color scale on left; scale bars represent 1 μm.

(J) Plot of open circuit voltage over 600 s.

(K–M) Chronopotentiometry plots corresponding to reduction cycle 1, oxidation cycle 1, and reduction cycle 2, respectively.

reduction and the weakening of V-O bands. Characteristic V L_{III}- and O K-edge spectral signatures at different extents of topochemical lithiation of ζ-V_2O_5 have been used as spectral standards to examine lithiation extents and inhomogeneities in individual ζ-V_2O_5 particles under HCDI conditions, using STXM (Figure 3, vide infra).

To directly connect the vanadium reduction observed in HAXPES and V L-XANES spectroscopy to insertion of Li ions,

Please cite this article in press as: Carrillo et al., Electrochemical ^{6}Li isotope enrichment based on selective insertion in 1D tunnel-structured V_2O_5, Chem (2025), https://doi.org/10.1016/j.chempr.2025.102486

Li K-edge XANES spectra have been acquired, and Δμ XANES spectra are plotted after subtracting the background spectrum measured for ζ-V_2O_5 (Figure 2G).[40]

$$\Delta\mu = \mu_{Lithiated} - \mu_{Reference} \quad \text{(Equation 1)}$$

Δμ XANES spectra show the differential change induced by lithiation as per Equation 1 where μ is the absorption coefficient. Careful normalization and subtraction of the reference spectrum in Δμ XANES eliminate the absorption features of the matrix and allow for isolation of Li K-edge features corresponding to surficial lithiation of ζ-V_2O_5.[41] Li K-edge XANES spectra reflect the excitation of Li 1*s* core electrons to hybrid 2*p* states. A pronounced feature at 62.4 eV is characteristic of ionic Li and is consistent with concomitant reduction of the ζ-V_2O_5 framework.[42,43] The broad feature at 63.9 eV results from the ionic interactions between the inserted Li ions and coordinated pendant oxygen atoms that line the edges of the 1D tunnel (Figure 1A).[42] The broadening is a result of phonon-driven structural distortions at finite temperatures.[44]

We next examine Li-ion insertion into ensembles of ζ-V_2O_5 particles[45,46] at a spatial resolution of ca. 25 nm, using operando X-ray spectromicroscopy, as shown in Figure 3A. Specifically, we have adapted an operando cell to flow an aqueous electrolyte through a three-electrode setup. We imaged a working electrode with affixed ζ-V_2O_5 particles by scanning across the V LIII-edge to probe the evolution of their spectral features in chronocoulometry experiments performed at constant reductive and oxidative currents. STXM stacks are collected before applying a potential, after chronocoulometry experiments flowing a 1 nA reductive and oxidative current (emulating a lithiation/delithiation cycle) and then after a second cycle with a 2 nA reductive and oxidative current. V LIII-edge XANES spectral signatures measured for topochemically lithiated ζ-V_2O_5 (Figure 2D) are used to interpret spectral evolution as a function of lithiation/delithiation and to construct single-particle composition maps. Figures 3B–3E show integrated X-ray optical density images, whereas Figures 3F–3I show composition maps inferred for each stack as per our previously published workflow.[38] The respective open circuit voltage and chronopotentiometry plots at different reductive and oxidative currents are plotted in Figures 3J–3M.

The initial open circuit voltage shows a potential difference between the ζ-V_2O_5 nanowire positive electrode and Pt anode, and an initial STXM image stack is acquired as a baseline (Figures 3B, 3F, and 3J). Initial reduction at 1 nA results in homogeneous lithiation up to a stoichiometry of about β-$Li_{0.20}V_2O_5$ (Figure 3G, corresponding spectra are shown in Figure S3B). The spectral changes corroborate faradaic processes resulting from insertion of Li ions within the 1D tunnels of ζ-V_2O_5. Upon subsequent oxidation, the particles are depleted of Li and reversibly oxidized back to the initial state (Figure 3H). The reversal of polarity corresponds to the release of previously sequestered Li ions in the form of an enriched brine stream. Upon reduction at a current of 2 nA, increased Li stoichiometries were observed in the composition maps (Figure 3I). The results provide compelling evidence for Li-ion sequestration from aqueous media occurring through faradic processes resulting from insertion of Li ions into the 1D tunnels of ζ-V_2O_5.

Li isotope enrichment

We next turn our attention to examining whether desolvation of Li ions at electrified interfaces and their solid-state diffusion through the 1D tunnels of ζ-V_2O_5 enforces isotopic selectivity. SIMS has been performed for a HCDI-recovered ζ-V_2O_5 positive electrode sample at full insertion and is compared with a $Li_{1.4}Al_{0.4}Ti_{1.6}(PO_4)_3$ standard. Figure 4B shows the signal intensities for ^{6}Li and ^{7}Li as a function of ablation depth and time. The intensities for both Li signals slightly increase with depth, likely as a result of surface cathode-electrolyte interface (CEI) formation. A consistent preference for ^{6}Li over ^{7}Li is observed with increasing depth. In contrast, the absolute intensities of both Li isotope signals remain largely constant as a function of depth for a $Li_{1.4}Al_{0.4}Ti_{1.6}(PO_4)_3$ standard (Figure 4C). The ^{6}Li/^{7}Li isotopic ratio determined from depth profiling experiments for the average of the material was 8.901% for Li ions inserted in the HCDI-recovered ζ-V_2O_5 positive electrode, as compared with 8.015% for the natural abundance $Li_{1.4}Al_{0.4}Ti_{1.6}(PO_4)_3$ standard.[47,48]

The HCDI-recovered ζ-V_2O_5 positive electrode (Table 1) and $Li_{1.4}Al_{0.4}Ti_{1.6}(PO_4)_3$ standard (Table S3) have been assayed 50 times across 3 different sputtered craters across distinct regions of electrodes at a depth of 1.5 μm to arrive at a more precise quantitative determination of the enrichment ratio. Table 1 displays the average ^{6}Li/^{7}Li isotopic ratio and standard deviation across six distinct sample spots at four different depths in the HCDI-recovered ζ-V_2O_5 positive electrode (Figure 4D shows an example of a sputtered crater). The areas surveyed are thus representative of the entire 2 mm × 2 mm electrode sample.

The SIMS measurement involves the detection of secondary positively charged ions of Li ejected because of the impact of a 5.5 keV O_2^+ primary ion. The number of ions sputtered per impact is denoted as the yield. Under equilibrium sputtering conditions, the ratio of yields of ^{6}Li and ^{7}Li is given by Equation 2:

$$\frac{Y1}{Y2} = \frac{c1}{c2}\left(\frac{M2}{M1}\right)^{m} \quad \text{(Equation 2)}$$

where Y1 and Y2 are the yields of ^{6}Li and ^{7}Li atoms, c1/c2 is the natural isotope ratio of ^{6}Li and ^{7}Li, and M1 and M2 are the masses (in amu) of ^{6}Li and ^{7}Li atoms, respectively. The parameter m ($0 < m < 0.4$) is chosen to ensure that the ratio of the effective yields Y1 (^{6}Li)/c1 to Y2 (^{7}Li)/c2 is greater than 1.[49]

In SIMS, a subset of the sputtered atoms is ionized as a result of local electron exchange processes; the probability of ionization depends on the ionization potential of the emitted ion. The measured isotope ratio does not depend on ionization potentials of ^{6}Li and ^{7}Li but is instead governed by average velocity differentials. The probability of ionization depends on the velocity as per Equation 3.[50,51]

$$P \propto e^{-\left(\frac{v0}{v}\right)} \quad \text{(Equation 3)}$$

Here, *v0* is the effective velocity of the atoms in the matrix (mostly oxygen for the ζ-V_2O_5 electrode sample) in a linear collision

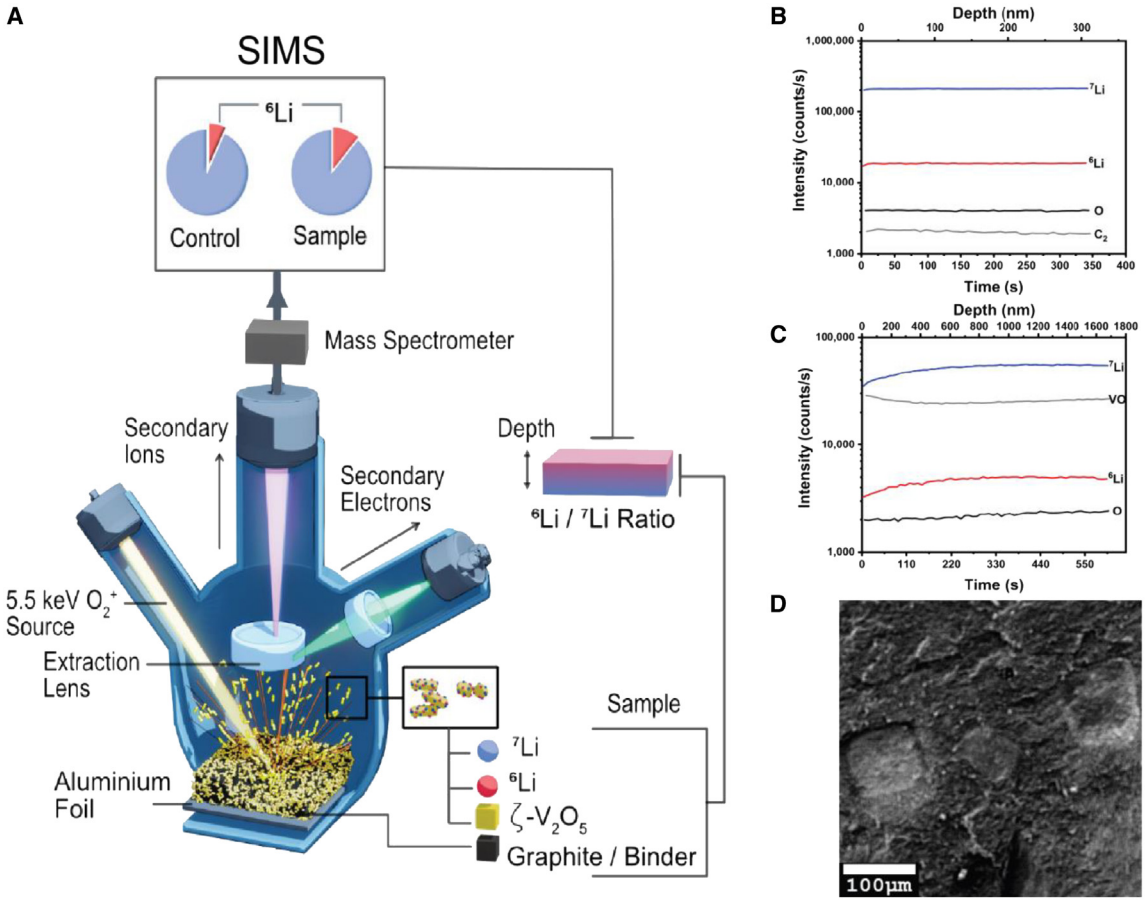

Figure 4. Isotope enrichment in HCDI cells

(A) Schematic representation of the SIMS experiment.

(B) Depth profile of standard $Li_{1.4}Al_{0.4}Ti_{1.6}(PO_4)_3$ sample (^{6}Li/^{7}Li isotopic ratio).

(C) Depth profile of HCDI-recovered ζ-V_2O_5 sample at full insertion.

(D) SEM image of 100 μm × 100 μm ablation craters (3 μm and 11 μm depth) of HCDI-recovered ζ-V_2O_5 sample. Scale bar represents 100 μm.

cascade, and *v* is the average velocity of Li atoms recoiled in the collision cascade. Combining Equations 2 and 3 yields Equation 4:

$$P = M1v1 = M2v2 = M0v0 \qquad \text{(Equation 4)}$$

where *v1* and *v2* are the average velocities of ^{6}Li and ^{7}Li, respectively.

Combining Equations 2, 3, and 4 gives the calculated model for isotope ratios in the SIMS experiment, as shown in Equation 5:

$$\left(\frac{N1}{N2}\right)^{model} = \frac{c1}{c2}\left(\frac{M2}{M1}\right)^{m} \frac{e^{-\left(\frac{\nu 0}{\nu 1}\right)}}{e^{-\left(\frac{\nu 0}{\nu 2}\right)}} = \frac{c1}{c2}\left(\frac{M2}{M1}\right)^{m} e^{\frac{M1-M2}{M3}}$$

(Equation 5)

Note that the SIMS method used here addresses some of the limitations of ensemble ICP-MS in Li isotope quantification, such as memory effects and isobaric nitrogen interferences. For the standard $Li_{1.4}Al_{0.4}Ti_{1.6}(PO_4)_3$ sample, carbon from the matrix is detected in abundance (M3 = 12 amu), and the calculated model ^{6}Li/^{7}Li ratio is 0.0898 (m = 0.2) (Table S2). The experimentally determined isotopic ratio of ^{6}Li/^{7}Li ratio in the $Li_{1.4}Al_{0.4}Ti_{1.6}(PO_4)_3$ standard is found to be 0.0899, indicating excellent agreement between the model and experiment (Table S3).

For the HCDI-recovered electrode sample, the model isotope ratio was calculated to be 0.0880 with the main matrix collision cascade comprising C atoms. This value is similar to the computed ratio for the reference $Li_{1.4}Al_{0.4}Ti_{1.6}(PO_4)_3$ sample. However, the measured intensity ratio for the electrode sample is 0.0950 (Table 1). This ratio is much higher than obtained for the standard sample, indicating partial ^{6}Li enrichment in the sample. From these ratios, an enrichment factor, δ, which is the quantitative value of ^{6}Li, can be calculated as per Equation 6:

$$\delta_{\frac{^{6}Li}{^{7}Li}} = 1,000\left[\frac{\left(\frac{N1}{N2}\right)^{electrode}}{\left(\frac{N1}{N2}\right)^{reference}} - 1\right] = 56.73‰ \qquad \text{(Equation 6)}$$

Please cite this article in press as: Carrillo et al., Electrochemical ^{6}Li isotope enrichment based on selective insertion in 1D tunnel-structured V_2O_5, Chem (2025), https://doi.org/10.1016/j.chempr.2025.102486

Table 1. Average ^{6}Li/^{7}Li ratio to recovered ζ-V_2O_5 HCDI positive electrode acquired at six distinctive samples

Sample	No. of measurements	Mean ^{6}Li/^{7}Li ratio	Standard deviation	Depth of measurement (μm)
Area a	50	0.095	0.0021	1.5
Area b	50	0.0952	0.0021	1.5
Area c	50	0.0949	0.0025	1.5
Average for 1.5 μm depth	150	0.0950	0.0022	–
Area d	20	0.0951	0.0027	3
Area e	20	0.0970	0.0025	3
Area f	20	0.0987	0.0033	3
Average for 3 μm depth	60	0.0969	0.0028	–
Area d	20	0.0947	0.0026	7
Area e	20	0.0947	0.0028	7
Area f	20	0.0947	0.0021	7
Average for 7 μm depth	60	0.0947	0.0024	–
Area d	20	0.0956	0.0024	11
Area e	20	0.096	0.0028	11
Area f	20	0.0987	0.0033	11
Average for 11 μm depth	60	0.0968	0.0028	–

Areas a, b, and c are distributed randomly across the available electrode and sampled to a depth of 1.5 μm. Areas d, e, and f are distributed approximately 300 μm apart from one another and sampled at three distinct depths of 3, 7, and 11 μm.

An enrichment factor of 56.73‰ demonstrates that ζ-V_2O_5 can be utilized as a discriminating host to selectively sequester and enrich ^{6}Li from natural abundance precursor flow streams. This enrichment brings ^{6}Li abundance from 7.59% to 8.02% in our enriched electrodes. This value is significant because similar separations (i.e., using crown ethers or ionic liquids) reported in the literature routinely fall short of δ greater than 50‰; the upper bound for the COLEX process is ≈δ = 60‰ at 0°C.[52,53] An additional metric used to assess separations is α, which is a single-stage fractionation metric. α is given by Equation 7:

$$\alpha_7^6 = \frac{\left(\frac{[6Li]}{[7Li]}\right)_{phase\ 1}}{\left(\frac{[6Li]}{[7Li]}\right)_{phase\ 2}} \qquad \text{(Equation 7)}$$

For our material, we have achieved an α = 1.06, which exceeds the α = 1.04 value of the incumbent COLEX process at 40°C. Alternative methods being developed, such as enrichment using biological processes, are notable for achieving δ > 85‰ but require significantly longer to enrich (28 days as compared with 4-h half-cycles using our process), require rigorously constrained conditions for microbial growth, and necessitate extensive extraction and separation steps to access the enriched Li.[54] From the perspective of scalability, it is worth noting that the ζ-V_2O_5 positive electrode is now commercially available in kilogram quantities. As broader perspective for the isotope selectivity metrics measured here, the minimum ^{6}Li enrichment required for use in nuclear fusion depends on the specifics of reactor design with a desired purity values range of (30 to 90)%.[55–57] Thus, minimum enrichment of 30% for fusion fuel can be achieved within 25 cycles and 90% enrichment within 45 sequential cycles. As noted in Figure 3, the sequestered Li ions can be released in the form of an enriched brine stream by reversal of polarity. Solid hydroxide or carbonate products can be isolated through conventional precipitation processes through addition of hydrated lime or soda ash or through methods such as electrodialysis with a bipolar membrane[58] or room-temperature CO_2 plasma precipitation of brines.[59–63]

We next examine the depth sensitivity of isotopic enrichment. ^{6}Li/^{7}Li measurements have been performed across three different craters defined within HCDI-recovered electrodes at depths of 3, 7, and 11 μm (Table 1). The mean ^{6}Li/^{7}Li ratios noted in Table 1, averaged across 20 measurements across 3 distinct spots, are consistent with the values measured at 1.53 μm, corroborating that the observed isotopic enrichment is consistent across the bulk of the material and does not merely reflect kinetic selectivity at interfaces. The 4-h half-cycles examined here and the 3,400 nm × 150 nm (L × W) dimensions of the ζ-V_2O_5 particles used to construct the primary electrodes imply that Li-ion sequestration in the porous electrodes is not diffusion limited. Indeed, Li-ion diffusion coefficients in porous ζ-V_2O_5 electrodes have been estimated using galvanostatic intermittent titration technique (GITT) to range from 3×10^{-9} to 1×10^{-12} cm^2s^{-1}, depending on the extent of lithiation.[22] Density functional theory (DFT) calculations indicate that the barrier for Li-ion migration in ζ-V_2O_5 is only ca. 0.14 eV (which reflects a diffusion coefficient of ca. 5×10^{-8} cm^2s^{-1}) but increases to ca. 0.50 eV with increasing lithiation.[64] As such, the measured isotope selectivity represents binding preferences in specific pseudocapacitive insertion and diffusion processes.

Figure 5A schematically illustrates the diffusion of hydrated Li ions to the electrode interface where they are bound through capacitive and pseudocapacitive processes before desolvation and insertion into the 1D tunnels of ζ-V_2O_5.[19,65] Video S1 shows an AIMD simulation of the motion of an individual hydrated Li

Please cite this article in press as: Carrillo et al., Electrochemical ^{6}Li isotope enrichment based on selective insertion in 1D tunnel-structured V_2O_5, Chem (2025), https://doi.org/10.1016/j.chempr.2025.102486

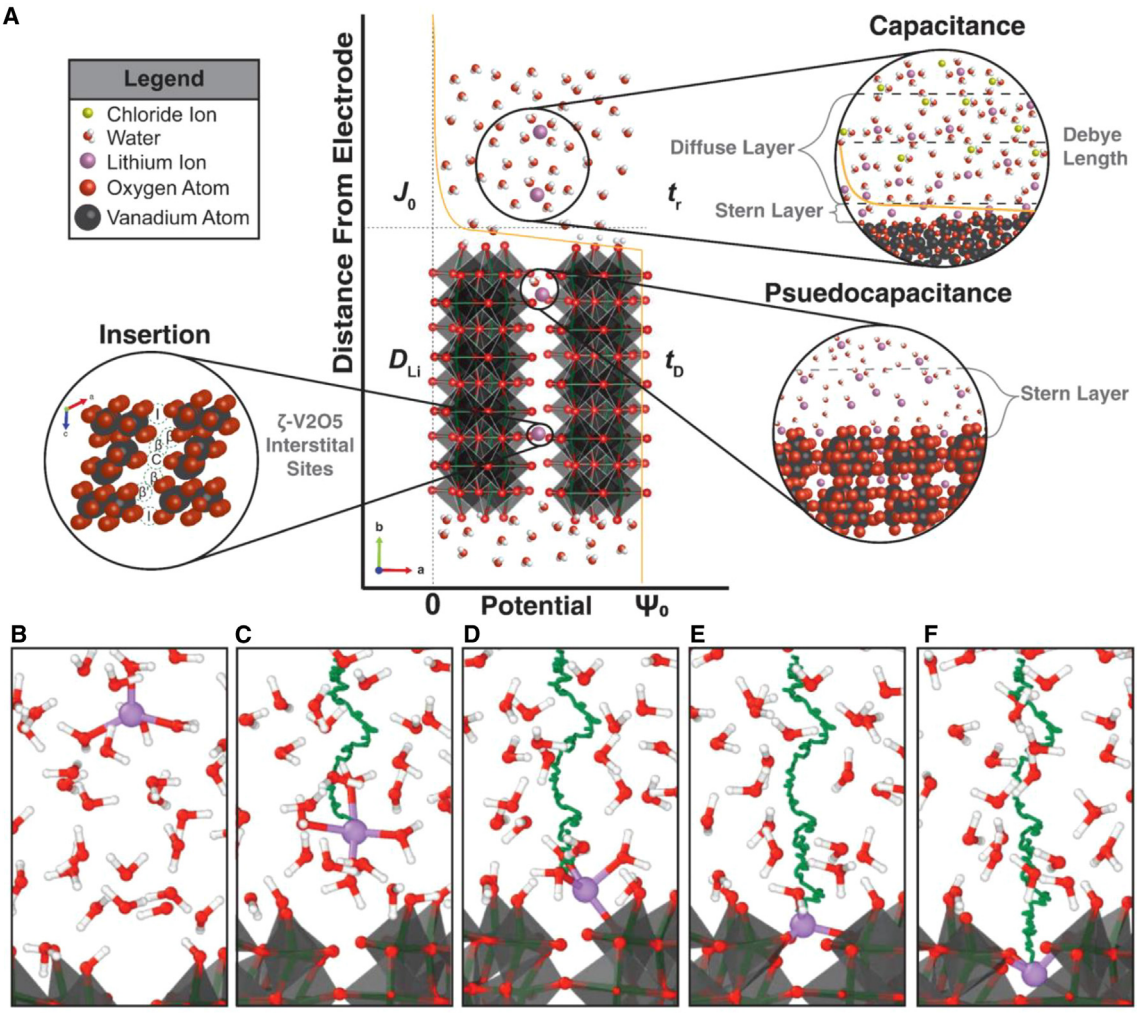

Figure 5. Desolvation and interfacial interaction of Li with ζ-V_2O_5

(A) Schematic representation of the diffusion of Li-ion and various electrochemical phenomena at the interface.

(B–F) Selected snapshots depicting the desolvation process of Li ions at the interface of ζ-V_2O_5. Desolvation is the primary rate-limiting step in Li-ion insertion into the host material.

ion in proximity to the electrified interface; the 1D tunnels of ζ-V_2O_5 are oriented perpendicular to the *ac* planes wetted by the aqueous electrolyte. Figures 5B–5F display snapshots from the simulation wherein the trajectory of the ion is marked in green. The simulation shows the extensive hydration of the Li ion in the Stern layer, which necessitates the displacement of a considerable number of water molecules as it moves toward the interface. Figure 5D shows the initiation of a ligand substitution reaction wherein water molecules are displaced by oxide moieties on the surfaces of ζ-V_2O_5. The stronger oxide ligands define a surface coordination environment that, along with the reduction of surface vanadium species, constitutes the pseudocapacitive process. The large hydration radius of ca. 3.8 Å and high hydration free energy of Li ions (515 to 544 kJ/mol[66]) result in slow desolvation and insertion (Figures 5E and 5F) processes; the reaction rate (t_r) is comparable to or slower than the diffusion rate (t_D). The 4-h cycle times used here ensure that the isotope selectivity reflects binding preferences. While a comprehensive examination of surficial and interfacial binding of hydrated Li ions on different possible surfaces of ζ-V_2O_5 is beyond the scope of this study, we have used AIMD simulations to examine the origins of selective ^{6}Li-ion sequestration in the 1D tunnels of ζ-V_2O_5.

The mobility of inserted Li ions is governed by the site preferences, occupancies, and local coordination environment encountered by Li ions in traversing through a periodic lattice. The site-to-site migration barrier for Li-ion diffusion is governed by the Li-O interactions at the interstitial sites sketched in Figure 1A and the geometry and energetics of the transition state for hopping between the interstitial sites.[67] Figure 6A shows Li-ion mobility at a low Li-ion loading, corresponding to β-$Li_{0.10}V_2O_5$. Based on mean square displacement (MSD) values, consistent "fast" Li diffusion is observed across all of the interstitial sites, as delineated by the sketched emerald-green trajectories. Figure 6B contrasts MSD profiles for ^{7}Li and

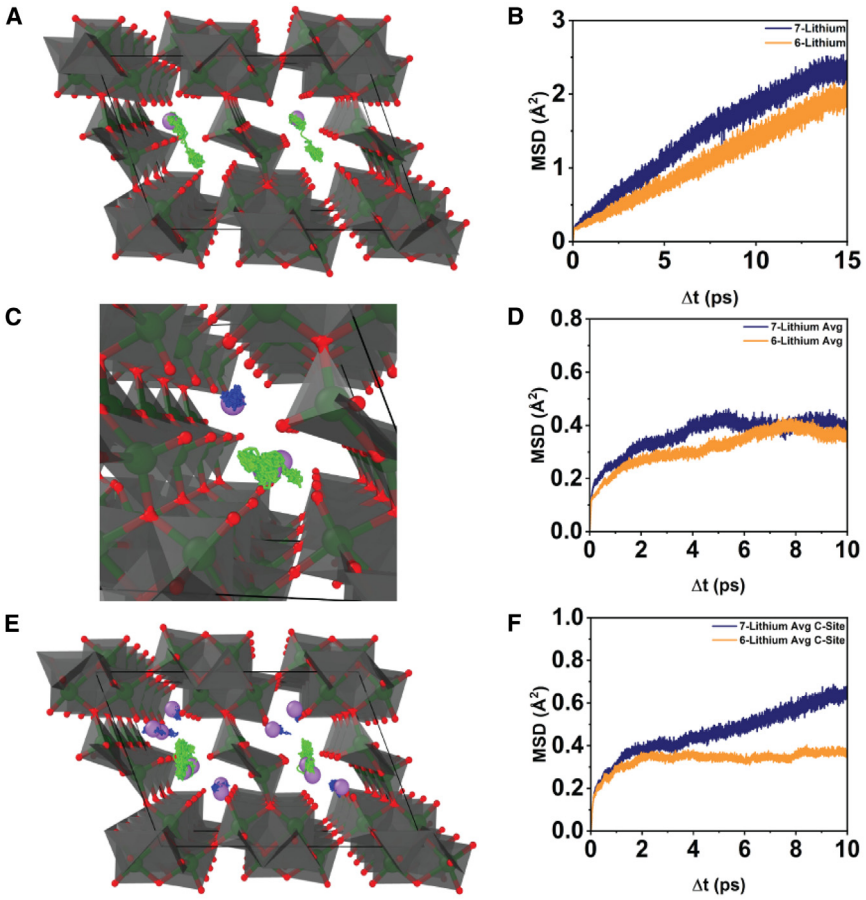

Figure 6. Simulations of Li-ion mobility

(A) Schematic illustration of Li-ion mobility at low Li-ion loading (β-$Li_{0.10}V_2O_5$), showing "fast" lithium diffusion across all interstitial sites (green trajectories).

(B) MSD profiles comparing ^{7}Li- and ^{6}Li-ion mobility in β-$Li_{0.10}V_2O_5$, with slightly greater mobility observed for ^{7}Li ions.

(C) Li-ion mobility at higher occupancy ($Li_{0.33}V_2O_5$), with decreased mobility for β and β' site Li ions (blue trajectories), compared with C site Li ions (green trajectories).

(D) MSD profiles at higher Li-ion loading, again showing greater mobility for ^{7}Li ions.

(E and F) Li-ion dynamics for β-$Li_{1.20}V_2O_5$, illustrating higher mobility of Li ions in C sites, compared with β and β' sites, and consistently greater mobility of ^{7}Li ions across varying Li-ion loadings.

^{6}Li ions in β-$Li_{0.10}V_2O_5$. In this insertion regime characterized by partial occupancy of β sites,[28] slightly greater mobility is observed for ^{7}Li ions; conversely, ^{6}Li ions are more likely to be retained. The greater mass of ^{7}Li ion compared with ^{6}Li ions induces a greater distortion of Li–O bonds under the same thermal excitation. This dynamic interaction between the Li ions and their local coordination environment can be conceptualized as per a simplified spring formalism represented in Equation 8:

$$\delta m_{Li} * a = - k_{bond} * \delta x \quad \text{(Equation 8)}$$

where δm_{Li} is the differential in isotopic mass, a is the acceleration factor from thermal effects, k_{bond} is the bond strength, and δx is the displacement. For a constant bond strength, thermal displacement is proportional to the isotopic mass. The greater thermal displacements of its proximate coordination environment by the heavier Li isotope underpins its greater mobility and lower persistence in the 1D tunnels of ζ-V_2O_5.

Figure 6C illustrates Li-ion mobility at a higher occupancy, corresponding to $Li_{0.33}V_2O_5$. With increasing occupancy of interstitial sites, Li ions within β and β' sites have a lower mobility (sketched as blue trajectories), as compared with Li ions in C sites (sketched as emerald-green trajectories). Figure 6D shows that ^{7}Li ions continue to have a slightly greater mobility than ^{6}Li ions ions even at these higher Li-ion loadings. Much of this mobility is mediated by fast ^{7}Li-ion diffusion through C sites at the center of the tunnel, whereas diffusion across β and β' sites along the edges of the tunnel is considerably slowed (Figure S4). Figures 6E and 6F plot Li-ion dynamics for β-$Li_{1.20}V_2O_5$ (see also Videos S2 and S3). Even at high Li-ion loadings, Li ions in C sites have a greater mobility, as compared with Li ions in β and β' sites along the edge of the tunnel (I sites between tunnels are not accessed until much higher Li-ion loadings[21]). The I site begins filling after β, β', and C sites are filled,[21] which occurs at a Li-ion stoichiometry of 1.66 Li per V_2O_5; ICP-MS shows maximum lithiation of 0.49 Li per V_2O_5 in our HCDI-recovered electrodes, and as such I-site mobility is not further considered. The greater mobility of Li ions across C sites compared with β and β' sites, together with the consistently greater mobility of ^{7}Li ions as compared with ^{6}Li ions, a pattern that is conserved across varying Li-ion loadings, suggests that ζ-V_2O_5 can selectively sequester ^{6}Li ions. Thus, ^{6}Li ions have a longer residence time than ^{7}Li ions, and their enrichment reflects the thermodynamic product at full insertion.

Conclusions

ζ-V_2O_5, a 1D tunnel-structured polymorph of V_2O_5, is known to selectively sequester Li ions from aqueous flow streams upon application of a voltage bias, thereby providing an effective means of direct Li extraction through HCDI. In this work, aided by comparison to topochemically lithiated ζ-V_2O_5 samples with well-defined Li stoichiometries, we use powder XRD and Raman spectroscopy to evidence that Li ions from aqueous flow streams are inserted within the 1D tunnels of ζ-V_2O_5 (and not just adsorbed on particle surfaces through capacitative and pseudocapacitative processes). Using a combination of core-level HAXPES and STXM, the latter interpreted with the aid of XANES measurements of topochemically lithiated standards, we demonstrate that ion extraction and storage are predominantly mediated by faradaic processes involving vanadium

Please cite this article in press as: Carrillo et al., Electrochemical ^{6}Li isotope enrichment based on selective insertion in 1D tunnel-structured V_2O_5, Chem (2025), https://doi.org/10.1016/j.chempr.2025.102486

reduction. A pronounced color change provides a colorimetric handle for monitoring state of charge in an integrated electrochemical resource recovery unit. *In situ* STXM measurements emulating the HCDI configuration illustrate increasing lithiation across ζ-V_2O_5 particles with increasing reductive current. The results demonstrate vanadium reduction across the particle volume, as Li ions are accommodated in interstitial sites within the 1D tunnel, manifested in the diminution of low-energy features at the V L_{III}-edge.

The strong ion selectivity of ζ-V_2O_5 derives from ion binding preferences in interstitial sites and from the migration barriers traversing across the 1D tunnel. This selectivity is shown by SIMS measurements to translate to a substantial selectivity for the ^{6}Li isotope, which is shown by depth profiling experiments to be consistent across the thickness of the electrode. An enrichment factor of 57‰ demonstrates that ζ-V_2O_5 can be utilized as a discriminating host to selectively sequester and enrich ^{6}Li from natural abundance precursor flow streams and is a substantial improvement over conventional COLEX processes. AIMD simulations demonstrate that the selectivity for ^{6}Li retention arises from the appreciably greater mobility of ^{7}Li ions across the center and edges of the 1D tunnels, which is consistently preserved at different Li-ion occupancies. The greater mobility of the heavier isotope is a manifestation of its ability to induce greater thermal displacement of its local coordination environment. Future work will examine the role of specific pulse sequences and cycle times in modification of isotope selectivity. Future work will further focus on site-selective modification of ζ-V_2O_5 through pre-intercalation and substitutional alloying to examine the modulation of mobility differentials between ^{6}Li and ^{7}Li.

METHODS

Synthesis of ζ-V_2O_5 nanowires

The synthesis of ζ-V_2O_5 was adapted from a previously reported method.[28] Briefly, 1 g of α-V_2O_5 (99.6% purity, Sigma-Aldrich) and 0.3333 g of silver acetate (99% purity, Thermo Scientific) were mixed using a pestle and mortar for 30 min. The mixture was added to a 123 mL polytetrafluoroethylene-lined pressure vessel (Parr), along with 80 mL of deionized water (ρ = 18.6 MΩ cm^{-1}) purified through Thermo Scientific GenPure UV/UF xCAD plus system. This mixture was heated in a laboratory oven (VWR Gravity Convection Oven, 89,511–412) at 210°C for 72 h, and then it was removed and allowed to cool to room temperature. The resulting green powder was isolated by vacuum filtration (Aceglass, 10 to 15 μm) and washed with deionized water and 2-propanol (99% purity, VWR) to yield 1.300 g of β-$Ag_{0.333}V_2O_5$. Next, 1.000 g of β-$Ag_{0.333}V_2O_5$ powder was added to a 123 mL polytetrafluoroethylene-lined pressure vessel (Parr), along with 78 mL of deionized water (ρ = 18.6 MΩ cm^{-1}) and 2.2 mL of an aqueous solution of 12 mol/L HCl (Avantor Performance Materials). This mixture was heated in an oven at 185°C for 24 h, and then it was removed and allowed to cool to room temperature. The resulting brown powder was recovered by vacuum filtration (Aceglass, 4 to 5.5 μm) and washed successively with an aqueous solution of 0.5 mol/L sodium thiosulfate, deionized water, and 2-propanol to obtain 0.725 g of ζ-V_2O_5 as a free-flowing orange powder.

Topochemical lithiation of ζ-V_2O_5

ζ-V_2O_5 nanowires were initially dispersed in 10 mL of dry acetonitrile (sigma, Drisolv ≥99.9% purity) within an Ar-filled glovebox. A 10% molar excess of the desired stoichiometric amount of anhydrous LiI (Sigma-Aldrich, 99.9% purity) was added to the ζ-V_2O_5 dispersion in acetonitrile, which was allowed to react for 72 h. Mole concentrations and their resulting ICP-MS-derived Li stoichiometries are listed in Table S1. Over the course of the reaction, the supernatant developed a brown/red color indicative of I_2 formation as per:

$$2\,\zeta - V_2O_5(s) + 2xLiI_{(MeCN)} \leftrightharpoons 2Li_xV_2O_5(s) + xI_{2\,(MeCN)}$$

(Equation 9)

Notably, I_2 acts as a mild oxidant and is sufficiently oxidizing to serve as a chemical deintercalation agent. Consequently, the topochemical lithiation process is best characterized as being reversible, and upon extended reaction times, it yields phase-pure powders of the target stoichiometries.[38] The resulting $Li_xV_2O_5$ powders were separated from the supernatant by allowing the solids to settle at the bottom of their respective fused silica vial and were decanted to recover the solid product. The dark green solid products were washed three times with dry acetonitrile to remove I_2 and excess unreacted LiI and subsequently decanted to recover the solid. The recovered powder was then left to dry in an Ar-filled glovebox (MBraun Labmaster 130) for 24 h before being ground using a mortar and pestle. After drying in a desiccator cabinet under an N_2 atmosphere for 24 h, phase purity of the recovered powder was confirmed by powder XRD.[38]

HCDI

Electrodes for HCDI were prepared by mixing 280 mg of the active material (ζ-V_2O_5 nanowires) and 80 mg of MTI Corporation Timical Super C45 conductive carbon black in a mixer mill for 1 h, then adding 0.5 mL mass fraction of 5% poly(vinylidene difluoride) (PVDF, MTI Corporation) in *N*-methyl-2-pyrrolidone (NMP, Thermo Scientific, 99.5% purity). The resulting slurry was stirred using a FlakTek speedmixer for 30 min at 262 rad/s, which yielded a homogeneous viscous slurry. The slurry was then cast onto Bralco battery-grade aluminum foil with a thickness of 15 μm using a casting knife (BYK) at a thickness of 0.125 mm. The cast electrodes were dried in a muffle furnace at 110°C for 15 min. Individual electrodes were cut from the electrode material to form 1 cm × 4 cm electrodes, each containing ca. 11 mg of the active material. A Li aluminum titanium phosphate standard ($Li_{1.4}Al_{0.4}Ti_{1.6}(PO_4)_3$, NEI Corporation) was produced using the same procedure as the ζ-V_2O_5 electrode, substituting $Li_{1.4}Al_{0.4}Ti_{1.6}(PO_4)_3$ for ζ-V_2O_5. In a control experiment, electrodes using α-V_2O_5 powder (Alfa Aesar) were prepared using the same procedure as the ζ-V_2O_5 electrode, substituting α-V_2O_5 for ζ-V_2O_5.

The negative electrode material for HCDI was prepared by mixing 280 mg of the active material (Strem Chemicals activated carbon with a surface area of [1,300 to 1,400] m^2/g) and 80 mg of Super C45 conductive carbon black, then adding 0.5 mL of 5 wt % PVDF in NMP. The resulting slurry was stirred using a FlakTek speedmixer for 30 min at 262 rad/s to prepare a homogeneous viscous slurry. The slurry was then cast onto

battery-grade aluminum foil with a thickness of 15 μm using a casting knife (BYK) at a thickness of 0.125 mm. The cast electrodes were dried in a muffle furnace at 110°C for 15 min. Individual electrodes were cut from the electrode material to form 1 cm × 4 cm counter-electrodes, each containing 11 mg of the active material.

An electrochemical deionization cell was constructed as depicted in Figure 1. This configuration pairs a carbon anode with the ζ-V_2O_5 positive electrode. The electrochemical cell was connected to a potentiostat (Gamry Interface 1010E Potentiostat/Galvanostat/ZRA), which served as the voltage source. An 80 mL reservoir solution of a 15 mmol/L aqueous solution of LiCl was circulated through the cell using a multichannel peristaltic pump (MINIPULS 3) at a flow rate of 20 mL/min. A repeating chronoamperometry experiment was initiated at a constant voltage of 1.2 V, reversing polarity in 4 h cycles. Changes in conductivity were measured by using a conductivity electrode (ET915, eDAQ) coupled with a conductivity isopod (EPU357, eDAQ) and plotted versus time. The conductivity electrode was calibrated using a series of LiCl standards, which were prepared from a 1-mol/L aqueous solution of LiCl with a series of dilutions using deionized water to a series of dilutions with 6 different concentrations, 4.7, 47, 95, 240, 495, and 5,400 mg/L. Changes in solution conductivity are interpreted as sequestration from and discharge of ions into the solution at the electrode. In a control experiment, α-V_2O_5 (Alfa Aesar, 99.6% purity) was substituted for ζ-V_2O_5, and the combined cell was cycled under the same conditions as above. Solution reservoir conductivity data for α-V_2O_5 were collected using 4 h half-cycles, while current density data for α-V_2O_5 were collected using 1 h half-cycles.

After electrochemical cycling, the experiment was halted at specific points (half insertion, full insertion, and half deinsertion) at which the HCDI cell was disassembled. The recovered electrodes were washed with copious amounts of deionized water to remove surface-adsorbed species. The washed electrodes were then carefully separated from the Al foil substrate by scraping the material using a stainless-steel spatula and transferred into a glass vial. These samples were dried in a muffle furnace at 110°C for 24 h in static, ambient air and recovered for further analysis to evidence modes and extents of Li sequestration.

Powder XRD

Powder XRD data were collected using a D8 Advances Ecol. instrument. The diffractometer was equipped with a Cu Kα radiation source (λ = 1.5418 Å) and utilized a Si-crystal zero diffraction plate with a diameter of 24.6 mm and a thickness of 1.0 mm.

ICP-MS

ICP-MS samples were analyzed using a PerkinElmer NexION 300D instrument at the Elemental Analysis Laboratory at Texas A&M University. Sample preparation entailed transferring (2 to 5) mg of solid powders into a 15 mL fluoroelastomer rubber tube and using 5 mL of nitric acid (≥65% to <70% purity, OmniTrace) and digesting at 80°C for (3 to 5) days in a digestion system (DigiPREP CUBE, SPC Science). Samples were then transferred into 50 mL VWR metal-free centrifuge tubes and diluted with deionized water to the 50 mL mark. Aliquots for each analyte (V and Li) were transferred to individual 50 mL metal-free centrifuge tubes and further diluted with a mass fraction of 1.5% HNO_3 aqueous solution. Dilutions were made to reach ultimate analyte concentrations within (100 to 200) μL/L, which are well within the detection limit of the instrument.

HAXPES

HAXPES measurements were performed at the 7-ID-2 (SST2) beamline of the National Synchrotron Light Source II of Brookhaven National Laboratory. Measurements were performed at approximately 2 keV photon energy with a pass energy of 200 eV and a step size of 0.85 eV, with the analyzer axis oriented parallel with the photoelectron polarization vector. Photon energy selection was accomplished using a double Si(111) crystal monochromator. The beam energy was aligned to the Fermi level of a silver foil prior to measurements.

XANES spectroscopy

V L- and O K-edge XANES spectroscopy measurements were carried out at the National Synchrotron Light Source II of Brookhaven National Laboratory beamline SST-1 operated by the National Institute of Standards and Technology. Measurements were performed in partial electron yield (PEY) mode with a nominal energy resolution of 0.1 eV. The PEY signal was normalized to the incident beam intensity using the photocurrent of a clean gold grid to eliminate the effects of any incident beam fluctuations and optics absorption features.

Li K-edge XANES measurements were carried out at the 11ID-2 VLS-PGM beamline of the Canadian Light Source in Saskatoon, Saskatchewan. The VLS-PGM beamline is equipped with an elliptically polarized Apple II type undulator, which provides an intense beam in the (15 to 250) eV energy range. Measurements were performed in total electron yield (TEY) mode with a nominal energy resolution of 0.1 eV. The TEY was divided by the I_0 and subsequently subtracted by the ζ-V_2O_5 Li-K XANES spectra to obtain the Δμ XANES.

STXM

STXM measurements were performed at the 10ID-1 beamline of the Canadian Light Source in Saskatoon, SK, CA. The 10ID-1 beamline is equipped with an elliptically polarized Apple II-type undulator, which provides an intense beam in the (130 to 2,700) eV energy range. State-of-the-art Fresnel zone plate optics are utilized in conjunction with an order-sorting aperture to achieve a focused X-ray beam. Regions of interest were defined to analyze hyperspectral data stacks. Regions of interest were initially identified using a single energy point at ca. 518 eV (corresponding to the V L_{III}-edge absorption) to achieve the highest contrast. Before initiating collection of spectromicroscopy hyperspectral stacks, a line-scan was typically performed to examine the integrated spectrum and assess the average composition based on the relative intensities of V L- and O K-edge features.[38] Next, the region of interest was raster-scanned while simultaneously recording transmission intensity in a stepwise fashion using a phosphor-scintillator-coupled photomultiplier tube (PMT) detector.

In situ STXM experiments were performed using the Hummingbird Scientific electrochemical setup, which utilizes two

SiN_x windows sandwiched together with a 30 μm × 200 μm window opening that allowed for transmission detection of sample under continuous electrolyte flow. A 1 mol/L aqueous solution of $LiNO_3$ (Sigma-Aldrich, ≥99.9% purity) was used as the electrolyte and flowed through the cell at a rate of 1 μL/min. Platinum was used as a counter-electrode and a standard calomel electrode was used as the reference electrode. The cell was then placed within the STXM instrument under ambient helium-backfill pressure. *In situ* STXM stacks were obtained in the energy range of (508 to 520) eV, corresponding to the V L_{III}-edge at a step size of 0.2 eV. *Ex situ* STXM hyperspectral stacks were obtained in the range from (508 to 560) eV corresponding to V-L and O-K edges. Stack sizes were acquired at a step size of 0.2 eV in the range of (508 to 560) eV, whereas post- and pre-edge spectra were collected with step sizes of 1 eV. Image registration and processing were achieved utilizing the cross-correlation analysis "Jacobsen stack analyze" function in the aXis2000 software suite (version April 22, 2023). An incident spectrum was extracted from a region corresponding to the transmission of the silicon nitride substrate and used in conversion of the overall transmission measurements to the optical density matrix. Principal-component analysis and subsequent k-means clustering were implemented utilizing the "PCA_GUI" routine (version 1.1.1) within the aXis2000 suite. The number of components considered for clustering was determined based on eigen values and their corresponding eigen spectrum/eigen image representation of the data. Previously measured standards aided the preliminary interpretation of eigen spectra, which furthermore enabled determination of the significant components.[25] The averaged spectrum from each cluster was compared with measured standards to assign Li stoichiometries for each cluster and subsequently used to obtain phase-specific signatures. Next, composition maps were generated by singular variable decomposition as per previously reported methods.[38]

Scanning electron microscopy

Scanning electron microscopy (SEM) images were acquired using a JEOL JSM-7500F instrument. Electrodes were cut from their current collectors and adhered to a SEM stub using double-sided copper tape. Standard instrument conditions for imaging were 5 kV accelerating voltage at a working distance of 8 mm.

Computational methods

The Vienna Ab initio Simulation Package (VASP, version 5.4.5) was utilized for structure optimization and AIMD simulations.[68,69] Structure solutions derived from single-crystal XRD, identifying Li interstitial sites in the tunnel-structured ζ-V_2O_5 polymorph, were used as initial inputs for the simulations and were optimized prior to performing AIMD simulations.[28] The generalized gradient approximation based on the Perdew-Burke-Ernzerhof functional (GGA-PBE) was used to describe the electronic exchange and correlation effects,[70] whereas the SCAN+U correction with a U_{eff} parameter set to 1.00 eV was implemented to capture electron correlation effects of V 3*d* electrons.[71] The projected augmented wave formalism was employed to model electron-ion interactions with a global break condition for the self-consistent iterative loop set to 10^{-4} eV.[72]

Structure optimizations were performed before the AIMD calculations, using a kinetic energy cutoff set to 520 eV with a convergence criterion of 0.05 eV/Å and a reciprocal Monkhorst-Pack grid of 0.05 $Å^{-1}$. For the extended AIMD simulations, a temperature of 295 K was maintained using the canonical NVT ensemble. The simulations used a time step set to 1.5 fs, an energy cutoff of 400 eV, and a computationally viable Γ-point grid density. Upon thermal stabilization, the constrained *ab initio* molecular dynamics (cAIMD) method was used for the calculation of the free-energy barrier at 295 K for Li-ion mobility along the *b* axis of the ζ-V_2O_5 structure.[21,72–74] The SHAKE algorithm set to a 0.002 Å/step increment was used to constrain the system onto a defined reaction path.[75] The trapezoidal rule was used to integrate the free-energy gradient.

SIMS

SIMS was performed using a CAMECA IMS 4f ion microprobe. Analyzed surfaces were sputtered by a 5.5 keV O_2^+ beam with a current of 0.24 μA. The diameter of the beam was ca. 2 μm. A 200 μm × 200 μm area was scanned for experiments at depths of 1.5 μm. A 100 μm × 100 μm area was scanned for measurements at 3, 7, and 11 μm. The angle of incidence of the beam (between surface and beam direction) was 36°. The measured secondary ions were positively charged. Ion signals were acquired for 50 μm × 50 μm areas at the center of the crater. Signals of ions for ^{6}Li and ^{7}Li isotopes (measured intensity ratios) were measured as 50 measurements for each of three areas at 1.5 μm. Three subsequent areas were scanned, and 20 measurements were taken at each different depth of 3, 7, and 11 μm for each area.

RESOURCE AVAILABILITY

Lead contact

Requests for further information and resources should be directed to and will be fulfilled by the lead contact, Sarbajit Banerjee (sbanerje@ethz.ch).

Materials availability

This study did not generate new unique materials.

Data and code availability

- Any additional information required to reanalyze the data reported in this paper is available from the lead contact upon request.

ACKNOWLEDGMENTS

This work was primarily supported by the National Science Foundation under DMR 1809866 and by the Texas A&M System Translational Investment Fund. Use of the TAMU Materials Characterization Facility (RRID: SCR_022202) is acknowledged. A portion of the research described in this article was performed at the Canadian Light Source (SM and VLS-PGM beamlines), a national research facility of the University of Saskatchewan, which is supported by the Canada Foundation for Innovation (CFI), the Natural Sciences and Engineering Research Council of Canada (NSERC), the Canadian Institutes of Health Research (CIHR), the National Research Council (Canada), the Canadian Institutes of Health Research, the Government of Saskatchewan, and the University of Saskatchewan. This research used resources of the National Synchrotron Light Source II, a US DOE Office of Science User Facility operated for the DOE Office of Science by Brookhaven National Laboratory. Portions of this research were conducted with the advanced computing resources provided by Texas A&M High Performance Research Computing. Commercial equipment, instruments, or materials are identified in this paper to specify the

experimental procedure adequately. Such identification is not intended to imply recommendation or endorsement by the National Institute of Standards and Technology, nor is it intended to imply that the materials or equipment identified are necessarily the best available for the purpose. H.K. acknowledges the support of the NSF under a Graduate Research Fellowship grant DGE: 2139772. We acknowledge support from the Qatar Research, Development and Innovation Council, Qatar National Research Fund (ARG01-0522-230270). We acknowledge the support of Emile A. Schweikert toward the SIMS measurements. We acknowledge the support of Dr. Binbin Lin and Prof. Dr. Bai-Xiang Xu at Technische Universität Darmstadt toward the development of the composition maps in this manuscript.

AUTHOR CONTRIBUTIONS

Conceptualization, J.L.C., A.A.E., S.P.-B., L.Z., and S.B.; methodology, J.L.C., A.A.E., S.V., C.W., C.J., D.A.F., L.Z., and J.W.; investigation, J.L.C., A.A.E., C.A.L., H.K., J.A.A., and A.M.; formal analysis, J.L.C., L.Z., S.P.-B., and S.V.; writing – original draft, A.A.E., J.L.C., C.A.L., H.K., S.P.-B., S.B., and S.V.; writing – review & editing, A.A.E., J.L.C., H.K., S.P.-B., S.B., C.J., H.B., and M.A.-H.; funding acquisition, S.B., H.B., and M.A.-H.; supervision, S.B., A.A.E., and J.L.C.

DECLARATION OF INTERESTS

The authors declare no competing interests.

SUPPLEMENTAL INFORMATION

Supplemental information can be found online at https://doi.org/10.1016/j.chempr.2025.102486.

Received: October 10, 2024
Revised: January 27, 2025
Accepted: February 12, 2025
Published: March 20, 2025

REFERENCES

1. El-Emam, R.S., Constantin, A., Bhattacharyya, R., Ishaq, H., and Ricotti, M.E. (2024). Nuclear and renewables in multipurpose integrated energy systems: A critical review. Renew. Sustain. Energ. Rev. *192*, 114157. https://doi.org/10.1016/j.rser.2023.114157.
2. Ham, C., Kirk, A., Pamela, S., and Wilson, H. (2020). Filamentary plasma eruptions and their control on the route to fusion energy. Nat. Rev. Phys. *2*, 159–167. https://doi.org/10.1038/s42254-019-0144-1.
3. Knaster, J., Moeslang, A., and Muroga, T. (2016). Materials research for fusion. Nat. Phys. *12*, 424–434. https://doi.org/10.1038/nphys3735.
4. Lewis, G.N., and Macdonald, R.T. (1936). The Separation of Lithium Isotopes. J. Am. Chem. Soc. *58*, 2519–2524. https://doi.org/10.1021/ja01303a045.
5. Brooks, S.C., and Southworth, G.R. (2011). History of mercury use and environmental contamination at the Oak Ridge Y-12 Plant. Environ. Pollut. *159*, 219–228. https://doi.org/10.1016/j.envpol.2010.09.009.
6. Badea, S.L., Niculescu, V.C., and Iordache, A.M. (2023). New Trends in Separation Techniques of Lithium Isotopes: A Review of Chemical Separation Methods. Materials *16*, 3817. https://doi.org/10.3390/ma16103817.
7. Murali, A., Zhang, Z.L., Free, M.L., and Sarswat, P.K. (2021). A Comprehensive Review of Selected Major Categories of Lithium Isotope Separation Techniques. Phys. Status Solidi A *218*, 2100340. https://doi.org/10.1002/pssa.202100340.
8. Pei, H., Yan, F., Liu, H., He, B., and Li, J. (2024). The selective complexation of crown ethers for lithium isotope separation: A critical review. Sep. Purif. Technol. *341*, 126857. https://doi.org/10.1016/j.seppur.2024.126857.
9. Cui, L., Gao, R., Zhang, Q., Jiang, K., He, H., Ding, W.-L., and Cheng, F. (2024). Benzo-15-Crown-5 Functionalized Ionic Liquids with Enhanced Stability for Effective Separation of Lithium Isotopes: The Effect of Alkyl Chain Length. ACS Sustain. Chem. Eng. *12*, 1221–1232. https://doi.org/10.1021/acssuschemeng.3c05171.
10. Ha, R., Liu, F., Li, J., He, M., Lan, J., Wang, B., Sun, J., Liu, X., Ding, X., and Shi, W. (2023). Calix[4]arene-Decorated Covalent Organic Framework Conjugates for Lithium Isotope Separation. ACS Appl. Mater. Interfaces *15*, 5657–5666. https://doi.org/10.1021/acsami.2c20309.
11. Black, J.R., Umeda, G., Dunn, B., McDonough, W.F., and Kavner, A. (2009). Electrochemical Isotope Effect and Lithium Isotope Separation. J. Am. Chem. Soc. *131*, 9904–9905. https://doi.org/10.1021/ja903926x.
12. Blair, J.W., and Murphy, G.W. (1960). Electrochemical Demineralization of Water with Porous Electrodes of Large Surface Area. Saline Water Convers. *27*, 206–223. https://doi.org/10.1021/ba-1960-0027.ch020.
13. Liu, Y., Wang, K., Xu, X., Eid, K., Abdullah, A.M., Pan, L., and Yamauchi, Y. (2021). Recent Advances in Faradic Electrochemical Deionization: System Architectures versus Electrode Materials. ACS Nano *15*, 13924–13942. https://doi.org/10.1021/acsnano.1c03417.
14. Ma, J., Zhou, R., and Yu, F. (2024). Hotspots and future trends of capacitive deionization technology: A bibliometric review. Desalination *571*, 117107. https://doi.org/10.1016/j.desal.2023.117107.
15. Wang, H., Liu, Y., Li, Y.Q., Xu, X.T., Lu, T., and Pan, L.K. (2024). Tailoring the electrode material and structure of rocking-chair capacitive deionization for high-performance desalination. Mater. Horiz. *11*, 5209–5219. https://doi.org/10.1039/D4MH00773E.
16. Zhang, C., He, D., Ma, J., Tang, W., and Waite, T.D. (2018). Faradaic reactions in capacitive deionization (CDI) - problems and possibilities: A review. Water Res. *128*, 314–330. https://doi.org/10.1016/j.watres.2017.10.024.
17. Jin, J., Li, M., Tang, M., Li, Y., Liu, Y., Cao, H., and Li, F. (2020). Phase- and Crystallinity-Tailorable MnO_2 as an Electrode for Highly Efficient Hybrid Capacitive Deionization (HCDI). ACS Sustain. Chem. Eng. *8*, 11424–11434. https://doi.org/10.1021/acssuschemeng.0c04101.
18. Xu, D., Wang, W., Zhu, M., and Li, C. (2020). Recent Advances in Desalination Battery: An Initial Review. ACS Appl. Mater. Interfaces *12*, 57671–57685. https://doi.org/10.1021/acsami.0c15413.
19. Fleischmann, S., Mitchell, J.B., Wang, R., Zhan, C., Jiang, D.-E., Presser, V., and Augustyn, V. (2020). Pseudocapacitance: From Fundamental Understanding to High Power Energy Storage Materials. Chem. Rev. *120*, 6738–6782. https://doi.org/10.1021/acs.chemrev.0c00170.
20. Nie, J., Islam, T., Roy, S.C., Li, D., Amin, R., Taylor-Pashow, K., Zhu, X., Feng, R., Chernikov, R., Pramanik, A., et al. (2024). Amorphous K–Co–Mo–S Chalcogel: A Synergy of Surface Sorption and Ion-Exchange. Small *20*, e2400679. https://doi.org/10.1002/smll.202400679.
21. Handy, J.V., Zaheer, W., Albers, R., Agbeworvi, G., Boyko, T.D., Bakhmoutov, V., Bhuvanesh, N., and Banerjee, S. (2023). Protecting groups in insertion chemistry: Site-selective positioning of lithium ions in intercalation hosts. Matter *6*, 1125–1139. https://doi.org/10.1016/j.matt.2023.01.028.
22. Luo, Y., Rezaei, S., Santos, D.A., Zhang, Y., Handy, J.V., Carrillo, L., Schultz, B.J., Gobbato, L., Pupucevski, M., Wiaderek, K., et al. (2022). Cation reordering instead of phase transitions: Origins and implications of contrasting lithiation mechanisms in 1D ζ- and 2D α-V_2O_5. Proc. Natl. Acad. Sci. USA *119*, e2115072119. https://doi.org/10.1073/pnas.2115072119.
23. Cool, N.I., James, R., Schofield, P., Handy, J.V., Bhatia, M., and Banerjee, S. (2023). Tunnel-Structured ζ-V_2O_5 as a Redox-Active Insertion Host for Hybrid Capacitive Deionization. ACS Appl. Mater. Interfaces *15*, 1554–1562. https://doi.org/10.1021/acsami.2c17800.
24. Scanlon, D.O., Walsh, A., Morgan, B.J., and Watson, G.W. (2008). An ab initio Study of Reduction of V_2O_5 through the Formation of Oxygen

Vacancies and Li Intercalation. J. Phys. Chem. C *112*, 9903–9911. https://doi.org/10.1021/jp711334f.

25. Horrocks, G.A., Parija, A., De Jesus, L.R., Wangoh, L., Sallis, S., Luo, Y., Andrews, J.L., Jude, J., Jaye, C., Fischer, D.A., et al. (2017). Mitigating Cation Diffusion Limitations and Intercalation-Induced Framework Transitions in a 1D Tunnel-Structured Polymorph of V_2O_5. Chem. Mater. *29*, 10386–10397. https://doi.org/10.1021/acs.chemmater.7b03800.
26. Greiner, S., Schwarz, B., Ringenberg, M., Dürr, M., Ivanovic-Burmazovic, I., Fichtner, M., Anjass, M., and Streb, C. (2020). Redox-inactive ions control the redox-activity of molecular vanadium oxides. Chem. Sci. *11*, 4450–4455. https://doi.org/10.1039/D0SC01401J.
27. Wheeler, L.M., Phan, T.L., Smeaton, M.A., Acharya, S., Hariyani, S., Alexander, M.E., Gonzalez, M.I., Miller, E.M., Mulder, D.W., Banerjee, S., et al. (2024). Tuning Optical and Electrical Properties of Vanadium Oxide with Topochemical Reduction and Substitutional Tin. Chem. Mater. *36*, 10483–10495. https://doi.org/10.1021/acs.chemmater.4c01557.
28. Handy, J.V., Luo, Y.T., Andrews, J.L., Bhuvanesh, N., and Banerjee, S. (2020). An Atomic View of Cation Diffusion Pathways from Single-Crystal Topochemical Transformations. Angew. Chem. Int. Ed. Engl. *59*, 16385–16392. https://doi.org/10.1002/anie.202005513.
29. Zheng, L., Tran, T.N.T., Zhalmuratova, D., Ivey, D.G., and Chung, H.-J. (2019). Colorimetric Voltmeter Using Colloidal Fe_3O_4@SiO_2 Nanoparticles as an Overpotential Alarm System for Zinc–Air Batteries. ACS Appl. Nano Mater. *2*, 6982–6988. https://doi.org/10.1021/acsanm.9b01464.
30. Stancovski, V., and Badilescu, S. (2014). In situ Raman spectroscopic–electrochemical studies of lithium-ion battery materials: a historical overview. J. Appl. Electrochem. *44*, 23–43. https://doi.org/10.1007/s10800-013-0628-0.
31. Horrocks, G.A., Likely, M.F., Velazquez, J.M., and Banerjee, S. (2013). Finite size effects on the structural progression induced by lithiation of V_2O_5: a combined diffraction and Raman spectroscopy study. J. Mater. Chem. A *1*, 15265–15277. https://doi.org/10.1039/c3ta13690f.
32. Kalha, C., Fernando, N.K., Bhatt, P., Johansson, F.O.L., Lindblad, A., Rensmo, H., Medina, L.Z., Lindblad, R., Siol, S., Jeurgens, L.P.H., et al. (2021). Hard X-ray photoelectron spectroscopy: a snapshot of the state-of-the-art in 2020. J. Phys. Condens. Matter *33*, 233001. https://doi.org/10.1088/1361-648X/abeacd.
33. Jeurgens, L.P.H., Cancellieri, C., Borgschulte, A., and Watts, J.F. (2024). Advancements and challenges of HAXPES for materials sciences and technologies. Surf. Interface Anal. *56*, 397–398. https://doi.org/10.1002/sia.7318.
34. Schofield, P., Luo, Y., Zhang, D., Zaheer, W., Santos, D., Agbeworvi, G., Ponis, J.D., Handy, J.V., Andrews, J.L., Braham, E.J., et al. (2022). Doping-Induced Pre-Transformation to Extend Solid-Solution Regimes in Li-Ion Batteries. ACS Energy Lett. *7*, 3286–3292. https://doi.org/10.1021/acsenergylett.2c01868.
35. Jahrman, E.P., Holden, W.M., Govind, N., Kas, J.J., Rana, J., Piper, L.F.J., Siu, C., Whittingham, M.S., Fister, T.T., and Seidler, G.T. (2020). Valence-to-core X-ray emission spectroscopy of vanadium oxide and lithiated vanadyl phosphate materials. J. Mater. Chem. A *8*, 16332–16344. https://doi.org/10.1039/D0TA03620J.
36. Maganas, D., Roemelt, M., Hävecker, M., Trunschke, A., Knop-Gericke, A., Schlögl, R., and Neese, F. (2013). First principles calculations of the structure and V L-edge X-ray absorption spectra of V_2O_5 using local pair natural orbital coupled cluster theory and spin-orbit coupled configuration interaction approaches. Phys. Chem. Chem. Phys. *15*, 7260–7276. https://doi.org/10.1039/C3CP50709B.
37. Andrews, J.L., Mukherjee, A., Yoo, H.D., Parija, A., Marley, P.M., Fakra, S., Prendergast, D., Cabana, J., Klie, R.F., and Banerjee, S. (2018). Reversible Mg-Ion Insertion in a Metastable One-Dimensional Polymorph of V_2O_5. Chem *4*, 564–585. https://doi.org/10.1016/j.chempr.2017.12.018.
38. Santos, D.A., Andrews, J.L., Lin, B., De Jesus, L.R., Luo, Y., Pas, S., Gross, M.A., Carillo, L., Stein, P., Ding, Y., et al. (2022). Multivariate hyperspectral data analytics across length scales to probe compositional, phase, and strain heterogeneities in electrode materials. Patterns (N Y) *3*, 100634. https://doi.org/10.1016/j.patter.2022.100634.
39. Tolhurst, T.M., Leedahl, B., Andrews, J.L., Marley, P.M., Banerjee, S., and Moewes, A. (2016). Contrasting 1D tunnel-structured and 2D layered polymorphs of V_2O_5: relating crystal structure and bonding to band gaps and electronic structure. Phys. Chem. Chem. Phys. *18*, 15798–15806. https://doi.org/10.1039/c6cp02096h.
40. Patridge, C.J., Love, C.T., Swider-Lyons, K.E., Twigg, M.E., and Ramaker, D.E. (2013). In-situ X-ray absorption spectroscopy analysis of capacity fade in nanoscale-$LiCoO_2$. J. Solid State Chem. *203*, 134–144. https://doi.org/10.1016/j.jssc.2013.04.008.
41. Ramaker, D.E., and Koningsberger, D.C. (2010). The atomic AXAFS and $\Delta\mu$ XANES techniques as applied to heterogeneous catalysis and electrocatalysis. Phys. Chem. Chem. Phys. *12*, 5514–5534. https://doi.org/10.1039/B927120C.
42. Wang, D., and Zuin, L. (2017). Li K-edge X-ray absorption near edge structure spectra for a library of lithium compounds applied in lithium batteries. J. Power Sources *337*, 100–109. https://doi.org/10.1016/j.jpowsour.2016.10.105.
43. Xie, X.Z., Kuang, H., Wiens, E., Deevsalar, R., Tunc, A., Purdy, S., Zuin, L., Tse, J.S., Mi, J.X., and Pan, Y. (2024). Synthesis of jadarite in the Li_2O–Na_2O–B_2O_3–SiO_2–NaCl–H_2O system: FTIR, Raman, and Li and B K-edge XANES characterizations and theoretical calculations. Eur. J. Mineral. *36*, 139–151. https://doi.org/10.5194/ejm-36-139-2024.
44. Pascal, T.A., Boesenberg, U., Kostecki, R., Richardson, T.J., Weng, T.-C., Sokaras, D., Nordlund, D., McDermott, E., Moewes, A., Cabana, J., et al. (2014). Finite temperature effects on the X-ray absorption spectra of lithium compounds: First-principles interpretation of X-ray Raman measurements. J. Chem. Phys. *140*, 034107. https://doi.org/10.1063/1.4856835.
45. Black, A.P., Sorrentino, A., Fauth, F., Yousef, I., Simonelli, L., Frontera, C., Ponrouch, A., Tonti, D., and Palacín, M.R. (2023). Synchrotron radiation based operando characterization of battery materials. Chem. Sci. *14*, 1641–1665. https://doi.org/10.1039/D2SC04397A.
46. Lim, J., Li, Y., Alsem, D.H., So, H., Lee, S.C., Bai, P., Cogswell, D.A., Liu, X., Jin, N., Yu, Y.S., et al. (2016). Origin and hysteresis of lithium compositional spatiodynamics within battery primary particles. Science *353*, 566–571. https://doi.org/10.1126/science.aaf4914.
47. De Laeter, J.R., Böhlke, J.K., De Bièvre, P., Hidaka, H., Peiser, H.S., Rosman, K.J.R., and Taylor, P.D.P. (2003). Atomic weights of the elements. Review 2000 (IUPAC Technical Report). Pure Appl. Chem. *75*, 683–800. https://doi.org/10.1351/pac200375060683.
48. Wieser, M.E., and Coplen, T.B. (2010). Atomic weights of the elements 2009 (IUPAC Technical Report). Pure Appl. Chem. *83*, 359–396. https://doi.org/10.1351/PAC-REP-10-09-14.
49. Sigmund, P. (1987). Mechanisms and Theory of Physical Sputtering by Particle Impact. Nucl. Instrum. Meth. B *27*, 1–20. https://doi.org/10.1016/0168-583X(87)90004-8.
50. Mann, K., and Yu, M.L. (1987). Effect of Chemical Bonding on Positive Secondary-Ion Yields in Sputtering. Phys. Rev. B Condens. Matter *35*, 6043–6050. https://doi.org/10.1103/physrevb.35.6043.
51. Yu, M.L., and Lang, N.D. (1986). Mechanisms of Atomic Ion Emission during Sputtering. Nucl. Instrum. Meth. B *14*, 403–413. https://doi.org/10.1016/0168-583X(86)90135-7.
52. Giegerich, T., Battes, K., Schwenzer, J.C., and Day, C. (2019). Development of a viable route for lithium-6 supply of DEMO and future fusion power plants. Fusion Eng. Des. *149*, 111339. https://doi.org/10.1016/j.fusengdes.2019.111339.
53. Symons, E.A. (1985). Lithium Isotope Separation: A Review of Possible Techniques. Sep. Sci. Technol. *20*, 633–651. https://doi.org/10.1080/01496398508060696.
54. Díaz-Alejo, H.M., López-Rodas, V., García-Balboa, C., Tarín, F., Barrado, A.I., Conde, E., and Costas, E. (2021). The Upcoming (6)Li Isotope

Requirements Might Be Supplied by a Microalgal Enrichment Process. Microorganisms *9*, 1753. https://doi.org/10.3390/microorganisms9081753.

55. Bradshaw, A.M., Hamacher, T., and Fischer, U. (2011). Is nuclear fusion a sustainable energy form? Fusion Eng. Des. *86*, 2770–2773. https://doi.org/10.1016/j.fusengdes.2010.11.040.
56. Nishio, S., Ohmori, J., Kuroda, T., Tobita, K., Enoeda, M., Tsuru, D., Hirose, T., Sato, S., Kawamura, Y., Nakamura, H., et al. (2006). Consideration on blanket structure for fusion DEMO plant at JAERI. Fusion Eng. Des. *81*, 1271–1276. https://doi.org/10.1016/j.fusengdes.2005.08.100.
57. Tobita, K., Nishio, S., Tanigawa, H., Enoeda, M., Isono, T., Nakamura, H., Tsuru, D., Suzuki, S., Hayashi, T., Tsuchiya, K., et al. (2009). Torus configuration and materials selection on a fusion DEMO reactor, SlimCS. J. Nucl. Mater. *386–388*, 888–892. https://doi.org/10.1016/j.jnucmat.2008.12.197.
58. Chen, X., Ruan, X., Kentish, S.E., Li, G., Xu, T., and Chen, G.Q. (2021). Production of lithium hydroxide by electrodialysis with bipolar membranes. Sep. Purif. Technol. *274*, 119026. https://doi.org/10.1016/j.seppur.2021.119026.
59. Jiang, Z.W., Li, M.T., Wei, C., Cao, Y.L., Li, X.B., and Deng, Z.G. (2023). Solidification behavior and environmental risk assessment of toxic elements on tailings from carbothermic reduction-magnetic separation of lead blast furnace slag. J. Min. Metall. B. *59*, 363–373. https://doi.org/10.2298/JMMB221022031J.
60. Poenitzsch, V.Z., Wei, R., Coulter, K.E., and Langa, E. (2019). High Power Impulse Plasma Source. Patent 10,440,808, patent application 14/944,017, 01/09/2025, and granted 10/08/2019.
61. Kim, S.-h., Yoon, H., Min, T., Han, B., Lim, S., and Park, J. (2024). Carbon dioxide utilization in lithium carbonate precipitation: A short review. Environ. Eng. Res. *29*, 230553. https://doi.org/10.4491/eer.2023.553.
62. Garcia, L.V., Ho, Y.-C., Myo Thant, M.M., Han, D.S., and Lim, J.W. (2023). Lithium in a Sustainable Circular Economy: A Comprehensive Review. Processes *11*, 418. https://doi.org/10.3390/pr11020418.
63. Battaglia, G., Berkemeyer, L., Cipollina, A., Cortina, J.L., Fernandez de Labastida, M., Lopez Rodriguez, J., and Winter, D. (2022). Recovery of Lithium Carbonate from Dilute Li-Rich Brine via Homogenous and Heterogeneous Precipitation. Ind. Eng. Chem. Res. *61*, 13589–13602. https://doi.org/10.1021/acs.iecr.2c01397.
64. Luo, Y., Handy, J.V., Das, T., Ponis, J.D., Albers, R., Chiang, Y.-H., Pharr, M., Schultz, B.J., Gobbato, L., Brown, D.C., et al. (2024). Effect of pre-intercalation on Li-ion diffusion mapped by topochemical single-crystal transformation and operando investigation. Nat. Mater. *23*, 960–968. https://doi.org/10.1038/s41563-024-01842-y.
65. Kohl, H.E., Larriuz, C.A., Ezazi, A., Al-Hashimi, M., Bazzi, H.S., and Banerjee, S. (2024). Electrified Enhanced Recovery of Lithium from Unconventional Sources. Chimia (Aarau) *78*, 845–854. https://doi.org/10.2533/chimia.2024.845.
66. Tansel, B. (2012). Significance of thermodynamic and physical characteristics on permeation of ions during membrane separation: Hydrated radius, hydration free energy and viscous effects. Sep. Purif. Technol. *86*, 119–126. https://doi.org/10.1016/j.seppur.2011.10.033.
67. Parija, A., Liang, Y., Andrews, J.L., De Jesus, L.R.D., Prendergast, D., and Banerjee, S. (2016). Topochemically De-Intercalated Phases of V_2O_5 as Cathode Materials for Multivalent Intercalation Batteries: A First-Principles Evaluation. Chem. Mater. *28*, 5611–5620. https://doi.org/10.1021/acs.chemmater.6b01006.
68. Kresse, G., and Furthmüller, J. (1996). Efficient iterative schemes for ab initio total-energy calculations using a plane-wave basis set. Phys. Rev. B Condens. Matter *54*, 11169–11186. https://doi.org/10.1103/PhysRevB.54.11169.
69. Kresse, G., and Hafner, J. (1993). Ab-Initio Molecular-Dynamics for Open-Shell Transition-Metals. Phys. Rev. B Condens. Matter *48*, 13115–13118. https://doi.org/10.1103/PhysRevB.48.13115.
70. Perdew, J.P., Burke, K., and Ernzerhof, M. (1996). Generalized gradient approximation made simple. Phys. Rev. Lett. *77*, 3865–3868. https://doi.org/10.1103/PhysRevLett.77.3865.
71. Long, O.Y., Gautam, G.S., and Carter, E.A. (2020). Evaluating optimal *U* for 3d transition-metal oxides within the SCAN+*U* framework. Phys. Rev. Mater. *4*, 045401. https://doi.org/10.1103/PhysRevMaterials.4.045401.
72. Kresse, G., and Joubert, D. (1999). From ultrasoft pseudopotentials to the projector augmented-wave method. Phys. Rev. B *59*, 1758–1775. https://doi.org/10.1103/PhysRevB.59.1758.
73. Bucko, T. (2008). Ab initio calculations of free-energy reaction barriers. J. Phys. Condens. Matter *20*, 064211. https://doi.org/10.1088/0953-8984/20/6/064211.
74. Bucko, T., and Hafner, J. (2010). Entropy effects in hydrocarbon conversion reactions: free-energy integrations and transition-path sampling. J. Phys. Condens. Matter *22*, 384201. https://doi.org/10.1088/0953-8984/22/38/384201.
75. Ryckaert, J.P., Ciccotti, G., and Berendsen, H.J.C. (1977). Numerical-Integration of Cartesian Equations of Motion of a System with Constraints - Molecular-Dynamics of N-Alkanes. J. Comput. Phys. *23*, 327–341. https://doi.org/10.1016/0021-9991(77)90098-5.